

Enabling photodetection electronics for fluorescent diamond based quantum sensing

Vladislav Serafimov

February 4, 2026

Contents

1 Foreword	3
2 Summary	4
3 Introduction	5
3.1 Background	5
3.2 Purpose of the assignment	6
3.3 Assignment specifications	6
3.4 Scope of work	6
3.4.1 Project boundaries	7
3.4.2 Goals	7
3.4.3 Deliverables	8
3.5 Methodology	8
3.6 Report outline	8
4 Functional design	10
4.1 Background knowledge	10
4.1.1 Spin states	10
4.1.2 Zeeman effect	10
4.1.3 Energy levels	10
4.2 Quantum protocols	11
4.2.1 CW-ODMR	11
4.2.2 T_1 relaxometry	12
4.2.3 Other pulsed protocols	13
4.3 Quantum sensing setup	13
4.4 Laser driver	13
4.5 Photodetection	14
4.5.1 Photodiodes	14
4.5.2 TIA design	15
4.5.3 Power requirements	16
4.6 Lock-in amplification	17
5 Technical design	19
5.1 Current driver	19
5.1.1 Pulsing sequences	19
5.2 Photodetector design	20
5.2.1 First iteration	20
5.2.2 Second iteration	21
5.2.3 Third iteration	25
5.2.4 Fourth iteration	26
5.2.5 Final CW-ODMR iteration	28
5.3 Photodetection simulation	29
5.3.1 First iteration	29
5.3.2 Second iteration	30
5.3.3 Third iteration	31
5.3.4 Fourth iteration	32
5.3.5 Final CW-ODMR iteration	33
5.4 Photodetection implementation	34
5.4.1 First iteration	34

5.4.2	Second iteration	35
5.4.3	Third iteration	35
5.4.4	Fourth iteration	35
6	Testing and results	37
6.1	Test goals	37
6.2	Test setup	38
6.2.1	Photodiode-model characterization	38
6.2.2	S-parameter characterization	39
6.2.3	Integration test	39
6.3	Results	40
6.3.1	Photodiode-model characterization	40
6.3.2	S-parameter characterization	43
6.3.3	Integration test	43
6.3.4	Additional integration test	45
6.4	Discussion	46
6.5	Known limitations	47
7	Conclusion	51
8	Recommendations	52
Appendices		54
A	Code	54
Glossary		58

Chapter 1

Foreword

Chapter 2

Summary

Quantum sensing is a developing technology with numerous applications in the real world. At present, there is a need for smaller and cheaper quantum sensors. The Applied Nanotechnology research group is one of the many organizations working on a setup with these criteria in mind. However, quantum sensing protocols do not use conventional electrical circuits for measurements, but instead use and manipulate light. Purely optical designs are not possible, which is why the light from the quantum setup needs to be translated to electrical signals. For this project, the student was tasked with solving the challenge of detecting low-intensity light by creating a compact and affordable photodetector. Furthermore, the integration of the different subsystems of the quantum sensing setup needed to be worked on. Using a methodological approach, in the form of the V-Model, the project was tackled and completed successfully. A working photodetector was built to be used for magnetic field measurements using one of the fundamental quantum sensing protocols, **Constant-Wave ODMR (ODMR)**. Later, the detector was upgraded to support T_1 measurements. Partial integration tests were done, but complete setup integration has been established as a future project. For high-frequency protocols, modifications to the biasing of the diode might need to be made. Additionally, higher sensitivity can be achieved by changing the p-i-n photodiode for an avalanche or and InGaAs diode, although it is going to significantly increase the cost of the sensing setup.

Chapter 3

Introduction

This chapter introduces the assignment, along with some foundational concepts of quantum sensing. Furthermore, it covers the methodology, goals and boundaries, which all help outline the trajectory of the project.

3.1 Background

Nitrogen Vacancy (**NV**) centers are imperfections in the atomic structure of diamonds [1]. The two types of **NV** centers are **NV0** and **NV-**, as seen in Figure 3.2, but the **NV-** structure is much more commonly used in quantum applications. These imperfections have the useful property of spin-dependent luminescence. This means that the spin of the **NV** center affects the frequency of the light emitted by the structure¹. Using this quality of the **NV** structure, different environmental metrics (e.g magnetic fields) can be measured.

The Applied Nanotechnology research group is working on a **NV**-center-based sensor setup, a high-level block diagram of which can be seen in Figure 3.1. There exist several quantum protocols, but the one this setup needs to support is called **CW-ODMR**. At its core, **Optically Detected Magnetic Resonance (ODMR)** is a set of protocols, which can detect magnetic fields based on the fluctuations in the fluorescence of **NV** centers [3]. **CW-ODMR** in particular involves exposing the **NV** center to a **Microwave (MW)** sweep while illuminating it with a constant light source. This is in contrast with **Pulsed ODMR (ODMR)** techniques, which use different **Transistor-Transistor Logic (TTL)** pulse schemes [4] to modulate the **MW** signal and the light source. Although **CW-ODMR** is the main focus of the research group at the moment, support for pulsed protocols is also desired for future quantum sensing research.

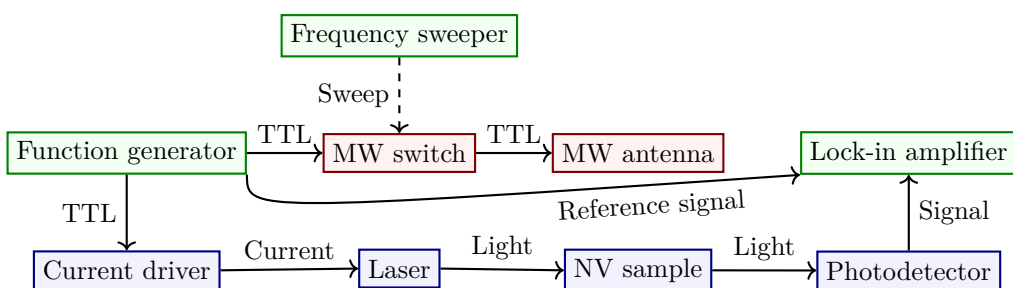


Figure 3.1: High-level overview of the quantum sensing setup

Acquiring and processing data from the setup requires working with weak signals that are hard to distinguish from the environmental noise. While this is a significant problem, it is also very common. Because of this, the industry has already adopted systems to detect weak light sources and measure their intensity. This project is mainly about developing a similar photodetection system for the **NV** setup.

¹The **NV** center only emits light after absorbing photons, a phenomenon called photoluminescence [2]

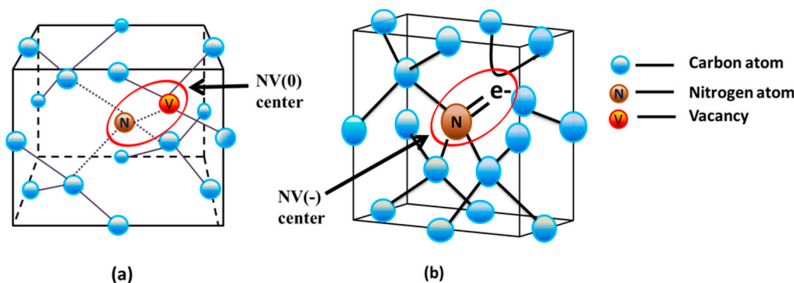


Figure 3.2: NV(0) (a) and NV- (b) structures in diamonds (image credit to Haque et al [5])

3.2 Purpose of the assignment

The main purpose of the assignment is to implement a photodetector. The quantum sensing setup is made up of other systems as well, which is why there are also several additional functionalities and systems that need to be developed.

Firstly, a custom photodetector needs to be designed. The circuit should output to a lock-in amplifier. After establishing connection, an **Open Lock-In Amplifier (OLIA)**² circuit needs to be tested and compared to conventional lock-in systems. Additionally, a control interface can be implemented, if there is enough time. It needs to be programmed so that it can control all necessary features of the lock-in amplifier. Aside from the data acquisition system, work also needs to be done on the existing current driver for the laser, as it needs to be tested at high frequencies and the pulsing sequences for it need to be programmed.

3.3 Assignment specifications

As already explained, the assignment is quite broad and involves both hardware and software, causing the need for a number of different tools.

Most of the hardware tools are already available at the Applied Nanotechnology lab. Most important of all is the equipment used for debugging the photodetector. Current and voltage supplies, along with oscilloscopes. The Zurich Instruments HF2LI is the benchmark lock-in amplifier. The target amplification is at least 10dB. Chapter 3.1 already discussed the basics of the **CW-ODMR** protocol. In order to get an operational **CW-ODMR** setup, an **MW** generator and a laser will be used. **MW** sweeping needs to be done in the range of 2,8 to 2,9 GHz and the lab already has a custom-built **MW** generator that can output these frequencies. The laser is mostly outside the scope of the assignment, as it is almost entirely optical in nature. The driving circuitry for it has been developed by a previous intern, but the integration with the sensing setup will be carried out in this project. The driver will be fed **TTL** pulse data from an Analog Discovery 2. It is important to note that the fluorescence wavelength is in the range of 637 to 800 nm, as it plays an important part in photodetection. It is different from the laser wavelength, which is filtered out and is not supposed to be detected by the photodetector. Lastly, FabLab equipment can be used when a tool is not available at the quantum lab.

In terms of software, there is more freedom of choice. Interfacing with the HF2LI is done through proprietary software. Similarly, pulse generation is going to be done with Waveforms, the Analog Discovery 2 software, but those are the only programs that cannot be replaced. As for **Electronic Computer-Aided Design (ECAD)** software, there are various suites that offer the same base functionality. KiCad was selected because the client prefers open-source software. The program for retrieving data from the lock-in amplifiers can be written in both Python and MATLAB. Both languages have good integration with the main lock-in amplifier. They also offer **Graphical User Interface (GUI)** programming capabilities and are good for scientific computing overall.

3.4 Scope of work

The scope of the project was extensively discussed with the company coach. Chapter 3.4.1 sets the scope and Chapter 3.4.2 builds on it, providing more specific details.

²6, **OLIA** is an open-source microcontroller-based lock-in amplifier. It uses common components, which makes it easy to build.

3.4.1 Project boundaries

The project boundaries were initially based on the assignment form, but were later discussed with the client and refined further.

Must have

- Hardware platform for photodetection
- Software for signal processing and visualization
- Setup integration

Should have

- Tests with different quantum protocols
- Tests with different diamond samples

Could have

- **OLIA** implementation
- Tests comparing **OLIA** to market solutions

Will not have

- Laser as a part of the hardware platform
- Laser driver upgrade

3.4.2 Goals

Based on the MoSCoW priorities from Chapter 3.4.1, a set of goals was created to further specify all items from each prioritization category. Every goal was designed so that its outcome results in a tangible project milestone (e.g. a deliverable).

Goal 1 : Create a hardware setup, which measures and amplifies photodiode signals

Goal 2 : Develop software to drive the laser and process lock-in amplifier signals

Goal 3 : Compare the performance of different lock-in amplifiers

While these goals are practical, they are still not specific enough. To eliminate the possibility of confusion, a set of tasks were created. All tasks contribute to one of the three goals.

Task 1.1 : Design a photodetector **Printed Circuit Board (PCB)**

Task 1.2 : Build an operable **OLIA**

Task 1.3 : Set up and test laser driver

Task 2.1 : Develop software that acquires signals and is then able to visualize them

Task 2.2 : Program quantum protocol pulse sequences for the laser driver

Task 3.1 : Use key performance metrics to compare the **OLIA** implementation to market solutions

Task 3.2 : Measure test setup performance using different diamond samples and quantum protocols

Task 1.1 involves the design and production of a photodiode **PCB**. The **PCB** has to output signals that are not only compatible with lock-in amplifiers that are available on the market, but also with the **OLIA** implementation. This part of the hardware design has the highest priority, which is why it will be done first.

Task 1.2 is to build an **OLIA** amplifier, which can be used at Applied Nanotechnology's laboratory. This will be done with the technical specifications and firmware provided by Harvie and de Mello [6]. The necessity for an **OLIA** is low, because the Applied Nanotechnology research group already has two lock-in amplifiers.

Task 1.3 is one of the more minor hardware tasks. As the driver is already designed and fabricated, it only needs to be tested and integrated with the rest of the setup. Tests should

show that the driver can switch the laser at high speeds, which is necessary for several quantum protocols.

Task 2.1 is to write an application in Python or MATLAB. This can be done on a different setup, but ideally it will use the hardware setup from **Goal 1**. Because the **OLIA** project uses open-source firmware that differs from proprietary solutions, there might need to be two separate applications. This task can only be completed once a measurement setup is built, so its execution will follow the first two tasks.

Task 2.2 makes sense only as a continuation of **Task 1.3**. Proper integration testing requires pulsing sequences, which will also be used when the setup is functional. These sequences are vital for the second stage of testing of the laser driver, so they need to be developed while the driver is still being tested with simple periodic signals.

Task 3.1 requires all previous tasks to be finished. The completed setup needs to be used to measure the performance of lock-in amplifiers available on the market and the **OLIA** implementation. **Signal-to-Noise Ratio (SNR)**, bandwidth and stability are the main metrics that need to be compared.

Task 3.2 is similar to **Task 3.1**, but it is a much broader in scope. Using different diamond samples and quantum protocols will show how the sensing setup performs and how different conditions affect it. Because the task can be used to verify the photodetector from **Goal 1**, it can also be done before **Task 3.1**. Tests with varying diamond samples are more important to the client, which is why they will take precedence over tests with different quantum protocols.

3.4.3 Deliverables

The description of the tasks already provided context for the deliverables, but this subsection contains a formalized version of the deliverables.

1. Photodetection **PCB**
2. **OLIA** implementation
3. Data acquisition application
4. Pulsing sequences
5. Technical documentation

The only deliverable, which was not mentioned in Chapter [3.4.2](#) is the technical documentation. This is because it should contain information about every task.

3.5 Methodology

The V-Model methodology was selected, as it is well-suited for low-level projects. Figure [3.3](#) shows a diagram of the phases of the V-Model. Unlike some software-oriented models, the V-Model is very sequential. This can sometimes be seen as detrimental, but in this case it helps with structuring the project. Another benefit of this model is that there are multiple testing activities, which underpin the quality assurance. A contentious feature of the V-Model is the heavy reliance on the initial requirements. This need for deliberate project requirements can be hard to meet, especially if the client representative is not technically proficient. However, this is not the case in this project. The requirements were extensively discussed with the client representative, based on which the project boundaries in Chapter [3.4.1](#) were set up.

3.6 Report outline

The introduction is followed by the functional design chapter, which introduces background knowledge, needed to understand the **NV** setup. After that, the high-level design of the system is presented. It explains the functionality of the various systems that make up the project without delving into specifics.

After that, the technical design explores the low-level design of the systems of the project. It mentions all the necessary details, including calculations, simulations and implementation steps.

Following the design sections, the testing chapter describes the testing goals and what methods were used for measuring. The chapter then presents the test results, followed by a short discussion of what they mean for the photodetector and the setup as a whole.

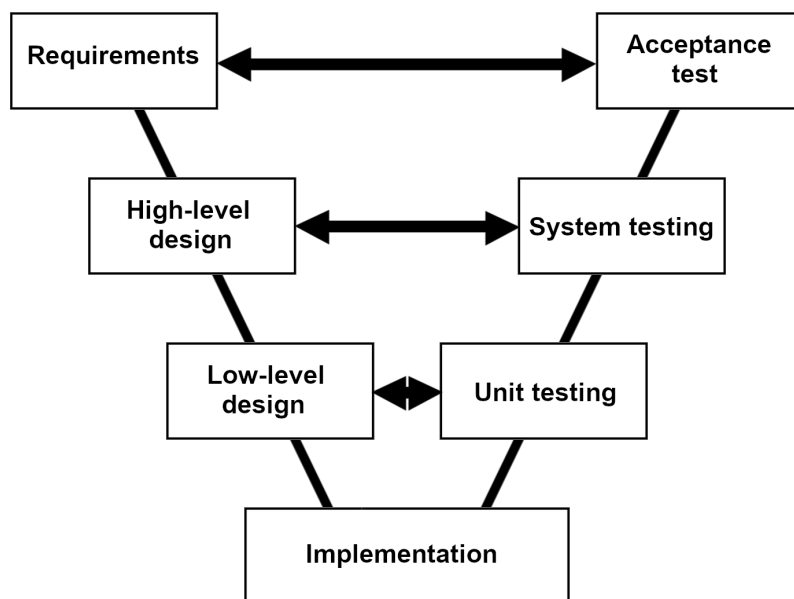


Figure 3.3: V-Model diagram

Lastly, the conclusion and recommendation chapters summarize the outcomes of the project and offer proposals for further development.

Chapter 4

Functional design

The functional design presents a high-level overview of the project and what explains what design choices were made on a system-level. Additionally, it provides tangential information that can be useful for understanding the working principle of the quantum sensing setup.

4.1 Background knowledge

Some background knowledge is required to understand the purpose of the projects, because the setup the project revolves around several non-trivial physics concepts. This section outlines the basic ideas behind the physics that enable the quantum sensing setup to work, from the fundamental physics to how it is used by protocols to detect magnetism.

4.1.1 Spin states

Spin, at least in quantum mechanics, is the intrinsic angular momentum of a particle, which is described by the quantum number of the particle. Importantly, it differs from the angular momentum in classical mechanics, which is extrinsic. Spin characterizes systems of particles, usually electrons, using quantum entanglement. This phenomenon refers to the "entanglement", or spin correlation, of a set of particles.

These foundational concepts make it possible to describe quantum systems using various states. The most simple states, used as descriptors, are the energy states. Ground states refer to the system being in an energy minimum. On the other hand, excited states signify that the system has more energy than at its ground state. Additionally, there can be intermediate states during state transition.

While the aforementioned states describe system energy, they have no bearing on the spin. For the purposes of this project, only two spin states need to be explained. The first one is called singlet state. It occurs when an entangled system has a total spin of 0, caused by the mutual cancellation of spin. For example, for a system of two entangled electrons to be a singlet, the two spins would need to point in opposite directions. The second spin state is called triplet and it has a total spin of 1. Triplets can consist of, for instance, two unpaired electrons with aligned spins that sum up to 1. Singlets and triplets both have major distinguishing features and properties, which is why they can be used for quantum sensing. Aside from the difference in spin, triplets tend to have higher energy levels. They also exhibit attraction to magnetic fields, while singlets cannot be influenced directly by magnetism.

4.1.2 Zeeman effect

Discovered by Pieter Zeeman in 1896, the Zeeman effect is another important phenomenon that enables quantum sensing. If under normal circumstances a light-emitting quantum system only emits one spectral line, then when a magnetic field is applied to it the line will split, thus exhibiting the Zeeman effect. In an NV center, this phenomenon causes the $|\pm 1\rangle$ energy level to split into $|+1\rangle$ and $| -1\rangle$.

4.1.3 Energy levels

Figure 4.1 shows the energy level diagram of an NV center.

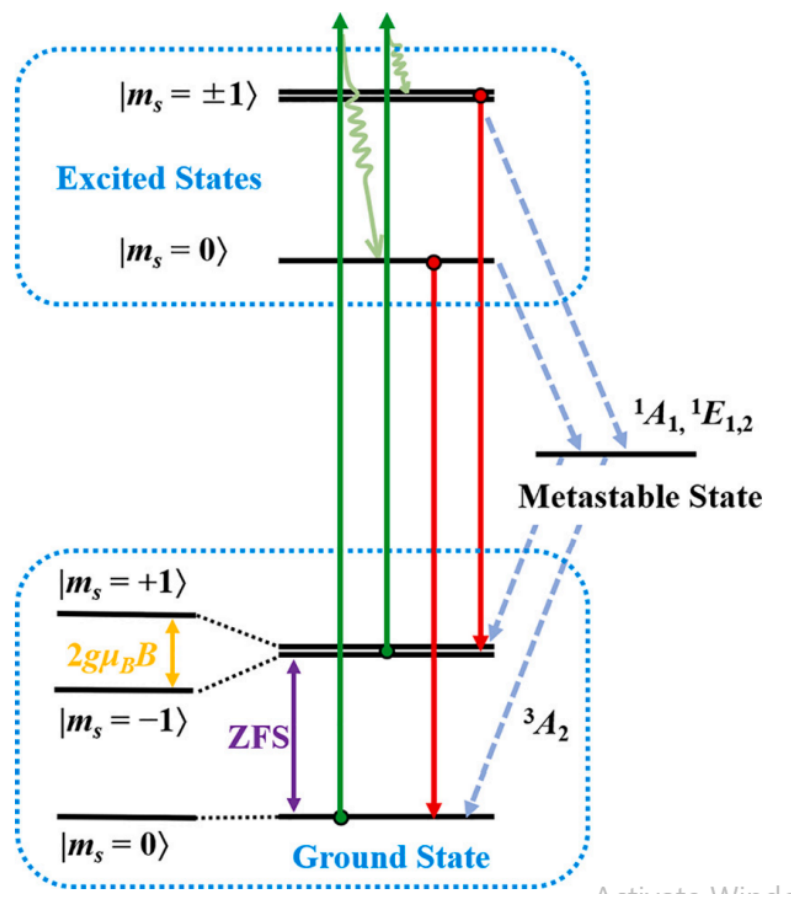


Figure 4.1: NV center energy level diagram (image credit to Song et al [7])

After illuminating the NV center with a green laser, electrons go from a ground state to an excited state. They then need to return to the ground state. This decay process is usually direct and emits a red photon, however it can also go through the metastable singlet state and emit an infrared photon. It should be noted that whenever the NV center is exposed to the resonant frequency $\nu = 2,87\text{GHz}$ the probability of emitting an infrared photon is significantly increased.

4.2 Quantum protocols

There are a number of different quantum protocols, which differ in what they can measure, in how precisely they can measure it and in the complexity of the hardware they require to operate. **CW-ODMR** is the main protocol this project is aimed at facilitating. As Saijo et al [8] demonstrate, **CW-ODMR** is relatively simple, while still detecting magnetic field with reasonable sensitivity. **P-ODMR** does outperform **CW-ODMR** [9], but because of the added complexity working with it is a "Could have" (see Chapter 3.4.1). Before being able to run **P-ODMR** on the setup at the lab, several protocols need to be implemented first [4]. T_1 measurements, which are one of the fundamentals of **Magnetic Resonance Imaging (MRI)**, should be conducted first. Afterwards, Rabi oscillations need to be observed and measured in order to calibrate the setup. Without these intermediate protocols, **P-ODMR** cannot be performed.

4.2.1 CW-ODMR

CW-ODMR is a quantum protocol that has seen extensive usage in sensing setups that measure magnetic fields. Its working principle is centered around the photoluminescence of NV centers and the difference in light emission based on spin states. As already discussed in Chapter 4.1.3, the NV center emits less visible light when at the resonant frequency ν . Additionally, two more dips appear on the spectrum if a magnetic field is applied. Calculating the magnetic field can be done using the formula $h\nu = g_e\mu_B B_{AC}$ ¹. Figure 4.2 shows an example of what a **CW-ODMR** spectrum

¹3, In the formula, h is the Planck constant, g_e is the g-factor of the electron and μ_B is the Bohr magneton. Knowing all other variables, B_{AC} can easily be calculated.

might look like.

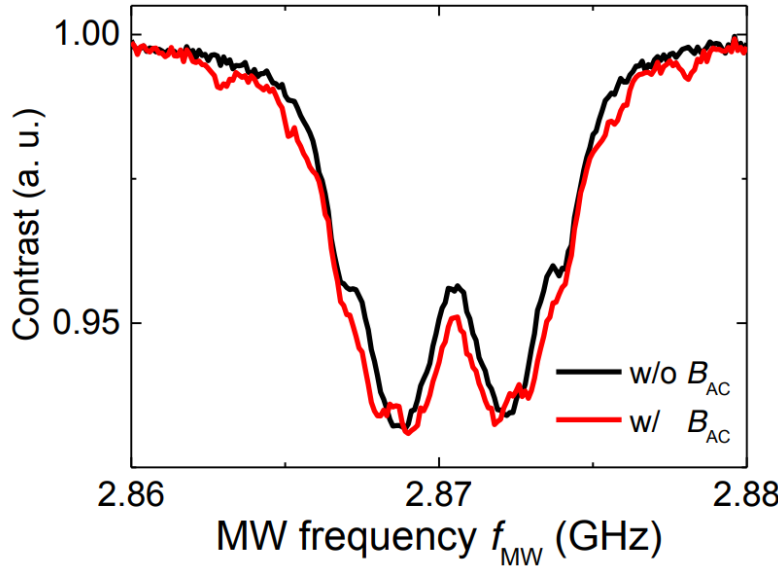


Figure 4.2: Example of a **CW-ODMR** spectrum **with** and **without** a magnetic field (image credit Sajio et al [8])

4.2.2 T_1 relaxometry

T_1 , T_2 and T_2^* relaxation time measurements are commonly associated with radiometry [10], but they have other uses too. T_1 measurements, in particular, are useful in the realm of quantum sensing. Knowing the T_1 relaxation time, which refers to the time it takes for the spins in an NV system to decay back to their original state, makes it possible to adjust the pulse sequences of more complex protocols and thus get better results.

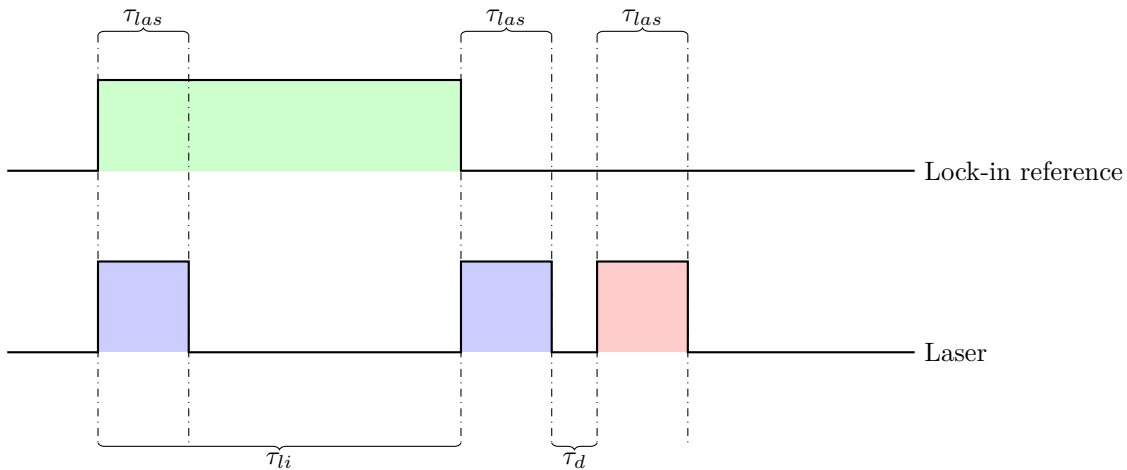


Figure 4.3: Laser and reference signals for T_1 measurements

The waveforms which are needed for T_1 measurements are shown in Figure 4.3. While both are important in practice, the lock-in is not as relevant, at least in this section of the report. However, its working principle is explored in Chapter 4.6. For now, all that needs to be said about the lock-in reference signal is that it is periodic and τ_{li} is much longer than τ_{las} (Sewani et al [4] propose $\tau_{li} = 15\text{ms}$ and $\tau_{\text{las}} = 5\mu\text{s}$). Laser pulses, on the other hand, are not periodic. Instead, there are three short pulses every reference period (which is $2\tau_{\text{las}}$ long). The two blue pulses have the same timing every cycle, because they initialize the NV spins. However, the red pulse always occurs after the variable dark time τ_d . Depending on the T_1 decay at the time of the readout pulse, a different voltage will be detected. Figure 4.4 shows what results can be expected when measuring T_1 . Determining the value of T_1 is done using Formula 4.1, where I is the light intensity, I_∞ is the light intensity offset and τ_d is the dark time.

$$I(t) = I_\infty + I(0)e^{-\tau_d/T_1} \quad (4.1)$$

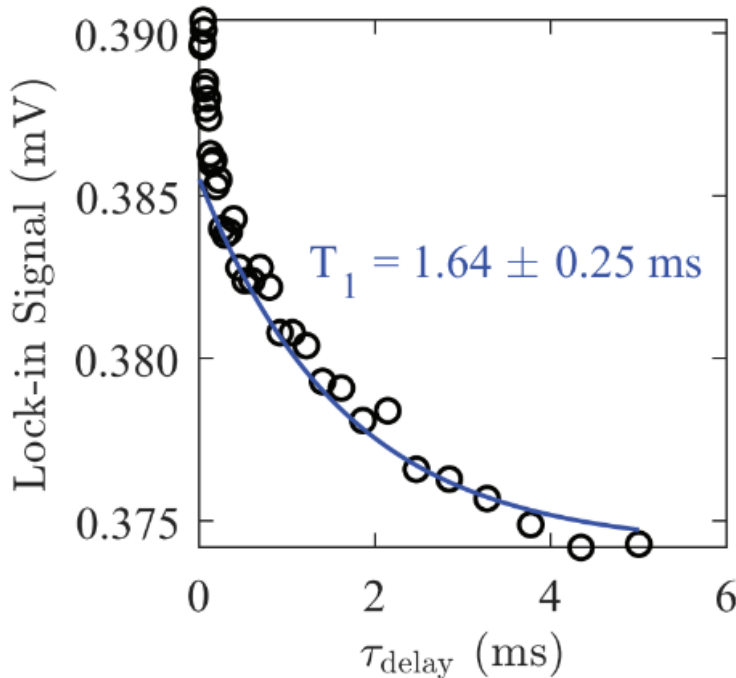


Figure 4.4: Results of a set of T_1 measurements with varied dark time τ_d (image credit to Sewani et al [4])

4.2.3 Other pulsed protocols

There are several protocols which fall under the **P-ODMR** umbrella. Aside from T_1 measurements, Ramsey interferometry, Hahn echo and Rabi oscillations are the most common pulsed protocols. Supporting Rabi oscillations is the ultimate goal of the quantum sensing setup at the Applied Nanotechnology research group. However, T_1 measurements need to be supported first, as based on them the quantum sensing setup will be optimized to detect Rabi oscillations.

4.3 Quantum sensing setup

Executing all of the aforementioned protocols requires a sensing setup with some specific capabilities. This section discusses the devices that make up the setup and the functionalities required by each protocol.

A high-level diagram of the quantum sensing system can be seen in Figure 3.1. There are 2 input devices in the system, but most protocols exclusively use the function generator. On the other hand, only a single lock-in amplifier is used as an output device for all measurements.

The blue boxes show the components responsible for sending and receiving light signals. They constitute the core of the setup. Voltage is generated by the function generator, no matter the protocol. Using a current driver, the laser is then used to illuminate the diamond sample. The resulting luminescence is then measured by the photodetector and processed by the lock-in amplifier. All protocols need this part of the setup, however they utilize it differently.

Microwave generation, when needed, starts with a **TTL** signal from the function generator or a frequency sweep using a dedicated device. Out of all protocols, only **CW-ODMR** requires a sweep. The antenna then broadcasts the signal, while the switch isolates the signal generator from it.

4.4 Laser driver

As discussed in Chapter 3.3, the laser driver has already been designed and built. It gets **TTL** signals from a waveform generator and outputs current to drive the connected laser.

However, the designer explicitly states that tests were only done with frequencies of up to 100 kHz [11]. This is insufficient for the project, as for example, the pulsing sequence for T_1 measurements use pulses with duration of 5 μs and downtime of as little as 1 μs ².

4.5 Photodetection

Photodetection is how the NV photoluminescence is measured, effectively turning light into current using a photodiode. However, a bare photodiode cannot be connected to a lock-in amplifier, because it functions as a current generator. This is where the photodetection PCB comes in. Its purpose is to transform the current into voltage and then amplify the resulting signal to the necessary voltage level.

4.5.1 Photodiodes

At the heart of the photodetector lies the photodiode. It is what turns light into current and feeds it into the Transimpedance Amplifier (TIA) that follows it. The specifications of the diode are an important part of the photodetector circuit. Photodiode biasing is another vital aspect of the photodetector, as it dictates the noise levels and bandwidth, thus directly influencing the amplifier design.

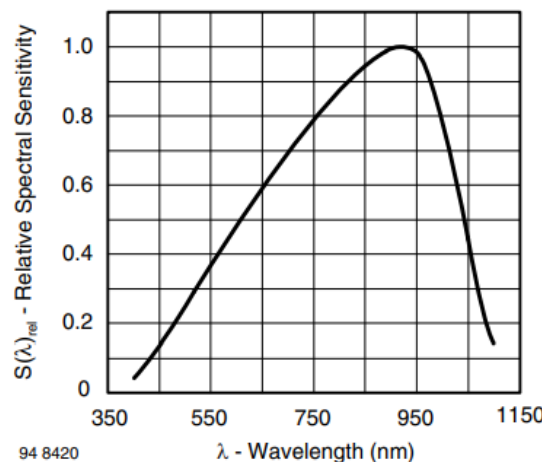


Figure 4.5: BPW34 sensitivity (image credit to the BPW34 documentation [12])

Figure 4.5 shows the sensitivity of the BPW34, which is the diode used in the setup. The green laser that is used to excite the NV centers has a wavelength of 550 nm. On the other hand, the light emitted from the NV centers has a wavelength of 637 to 800 nm, which is near the most sensitive wavelength range of the sensor. Although green light is not detected as well as red and infrared light, the much higher intensity of the laser means that an optical low-pass filter is required to measure the NV center luminescence. After filtering, the client said they expected less than 50 nA of photocurrent output, which they wanted to be translated to 0 to 5 V.

The two most common photodiode modes used in photodetectors are shown in Figure 4.6. Reverse-biased circuits, similar to the one in Figure 4.6a, are used in optical receivers and other high-speed use cases. However, the drawback of biasing the diode using the negative supply voltage V_{EE} is that it results in an increased dark current, which is current that, unlike photocurrent, runs through the diode without any light being present. In the case of the BPW34, that dark current is usually 2 nA, but in the worst case it can be up to 30 nA. That much current can render the amplified signal unreadable. Precise low-light measurements, such as those expected from the quantum setup, require the photodetector to have high linearity, which cannot be achieved when the dark current is comparable to the photocurrent. Photovoltaic-mode biasing reduces the dark current at the cost of signal strength and bandwidth [13]. This configuration is much more common in low-illumination setups, where the signals can be in the nanoampere to picoampere range. As the photoluminescent NV centers emit extremely low amounts of light, the photovoltaic configuration was chosen for the photodetector implementation for the quantum sensing setup.

²These values are taken from Sewani et al [4], but the clients wants to make the timings used by the quantum sensing setup even faster

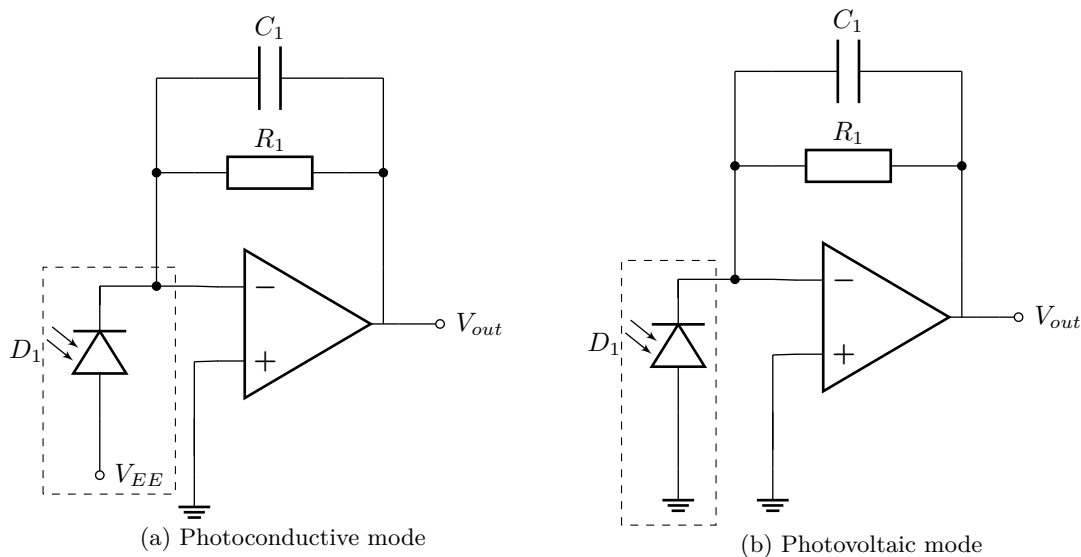


Figure 4.6: Photodiode modes in a photodetector circuit

4.5.2 TIA design

Designing the photodetector is mostly about creating a **TIA**, which is a tool used for converting current to voltage, and specifically tuning its parameters so that it works with the selected photodiode under operating conditions.

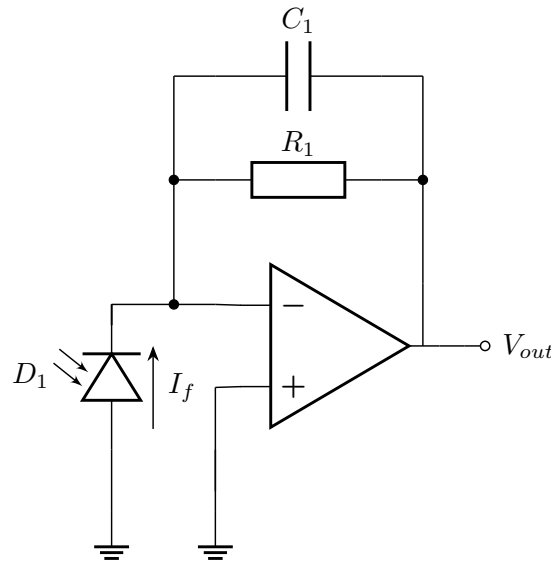


Figure 4.7: Basic TIA circuit

The basic circuit, shown in Figure 4.7, is all that is required for photodetection. Following the Texas Instruments guidelines for making a TIA [14], all the parameters of the circuit can be calculated.

$$R_1 = \frac{V_o \max}{I_f \ max} \text{ assuming } V_o \ min = 0\text{V} \quad (4.2)$$

The resistor R_1 determines the transimpedance gain of the amplifier. Equation (4.2) shows how its value can be calculated by using the output voltage and input current. It should be noted that the minimum output voltage is always 0 in this use case.

$$C_1 = \frac{1}{2\pi R_1 f_{rc}} \quad (4.3)$$

The ideal capacitance of C_1 can be calculated using the resistance of R_1 and the cutoff frequency f_{rc} , as shown in Equation (4.3). To select a physical capacitor based on the calculated value, its

capacitance should be less than or equal to the ideal value.

In addition, a non-inverting amplifier can be added, to increase the gain of the circuit even more, without affecting the phase. Figure 4.8 shows how it can be connected to the output of the TIA from Figure 4.7.

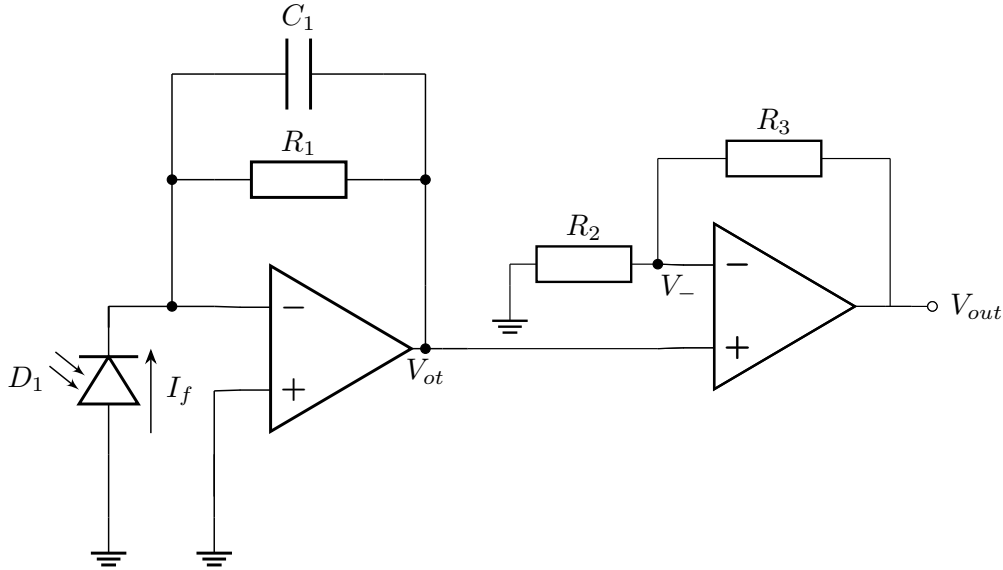


Figure 4.8: TIA with non-inverting output amplification

Equation (4.4) is used to calculate the gain of second amplification stage. The formula is derived from the voltage divider formed by the two resistors and the fact that $V_{ot} = V_-$.

$$A_{nia} = \frac{V_{out}}{V_{ot}} = 1 + \frac{R_3}{R_2} \quad (4.4)$$

The design is based on circuits provided by the client. At their request, the first version of the PCB is an exact replica of the original circuit.

4.5.3 Power requirements

Knowing the power needs of the photodetector is important for decreasing the size of the quantum setup. As bench power supplies take up a lot of space and exceed the photodetector requirements by orders of magnitude, an on-board supply or a breakout board will better fit the project. To minimize overhead while still having a supply that can handle the circuit, the power usage of the photodetector needs to be calculated.

When calculating the power of the circuit in Figure 4.8, the most important elements to consider are the op-amps. As the non-inverting amplifier has high input impedance, the system can be broken down into two op-amp circuits.

The op-amp in the TIA circuit has an intrinsic power dissipation caused by its quiescent current, as well as a load power dissipation. Due to the very high input impedance of the non-inverting topology that follows the TIA, there is no load current. Nevertheless, the feedback loop still draws a current $I_{f\alpha}$ from the amplifier. Equation (4.5) shows how this current can be calculated, after which the feedback power dissipation $I_{f\alpha}$ can be determined using Equation (4.6). It should be noted that for $C_1 R_1 \ll 1$ the equivalent impedance Z_1 is equivalent to the resistance R_1 at low frequencies.

$$\begin{cases} I_{f\alpha} = \frac{V_{ot}}{Z_1} \\ Z_1 = R_1 \parallel (\frac{1}{sC_1}) = \frac{R_1}{1+sC_1 R_1} \end{cases} \quad (4.5)$$

$$P_{f\alpha} = (V_{cc} - V_{ot})I_{f\alpha} \quad (4.6)$$

As a characteristic of the amplifier **Integrated Circuit (IC)**, the quiescent current $I_{q\alpha}$ can be taken from the datasheet to calculate its power dissipation $P_{q\alpha}$ with the formula shown in Equation (4.7).

$$P_{q\alpha} = (V_{cc} - V_{ee})I_{q\alpha} \quad (4.7)$$

Ultimately, the total power dissipation P_α of the TIA can be calculated by summing the results of the previous equations (see Equation (4.8)).

$$P_\alpha = P_{f\alpha} + P_{q\alpha} \quad (4.8)$$

Similarly to the amplifier that was just discussed, the non-inverting op-amp has a quiescent power dissipation $P_{q\beta}$ and a load power dissipation $P_{f\beta}$. It should be noted that even though V_{out} is not connected to in Figure 4.8, the output of the photodetector in the sensing setup needs to be connected to a lock-in amplifier. Even then, the load current that runs through it is imperceptibly low, which is why the power in Equations (4.9) and (4.10) is calculated in a similar way.

$$I_{f\beta} = \frac{V_{out} - V_{ot}}{R_3} \quad (4.9)$$

$$P_{f\beta} = (V_{cc} - V_{ee})I_{f\beta} \quad (4.10)$$

Equation (4.11) shows the quiescent power dissipation, which again is based on the intrinsic characteristics of the op-amp and combining all powers again yields the total power dissipation P_β of the amplifier, shown in Equation (4.12).

$$P_{q\beta} = (V_{cc} - V_{ee})I_{q\beta} \quad (4.11)$$

$$P_\beta = P_{f\beta} + P_{q\beta} \quad (4.12)$$

Additionally, the power dissipated by R_2 is given in Equation (4.13).

$$P_2 = V_{ot}I_{f\beta} \quad (4.13)$$

4.6 Lock-in amplification

As a means of retrieving data, lock-in amplification is the most suitable for the setup due to its relatively low cost, signal retrieval capabilities and the possibility of using one amplifier for several setups.

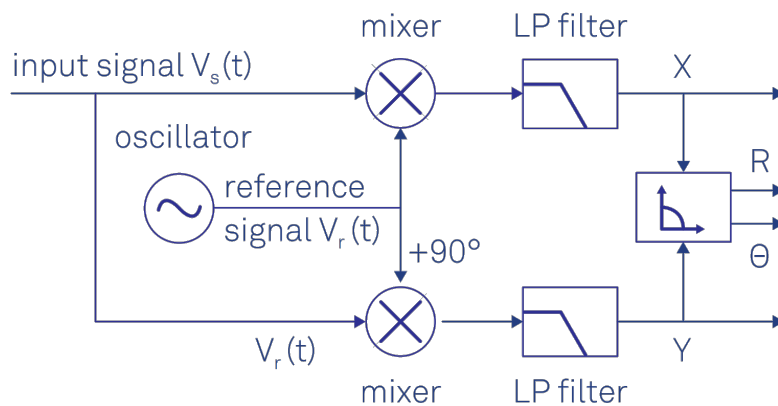


Figure 4.9: High-level diagram of a lock-in amplifier (image credit to Zurich Instruments [15])

Figure 4.9 shows an overview of how lock-in amplification works. Simply put, the amplifier receives a signal V_s and extracts the data at the frequency of a reference signal V_r . To explain this more thoroughly, lock-in amplification utilizes the fact that every signal is made of periodic waves, which are equal to zero when averaged.

$$V_s = R \cos(\omega_s t + \theta) = \frac{R}{2} e^{i(\omega_s t + \theta)} + \frac{R}{2} e^{-i(\omega_s t + \theta)} \quad (4.14)$$

Equation (4.14) shows how the mathematical expression of a sine wave signal, where ω_s is the frequency and θ is the phase of the signal. Using the trigonometric identity $\cos x = \frac{1}{2}(e^{ix} + e^{-ix})$, the signal can be represented in terms of complex numbers.

$$V_r = e^{-i\omega_r t} \quad (4.15)$$

In Equation (4.15), a simplified reference signal is shown. Real applications might require more complex reference signals, but V_r is perfect for demonstrating the lock-in principle.

$$V_m = V_s V_r = \frac{R}{2} e^{i(\omega_s - \omega_r)t + \theta} + \frac{R}{2} e^{-i(\omega_s + \omega_r)t + \theta} \quad (4.16)$$

Finally, Equation (4.16) shows the product of the signal V_s and the reference V_r . In the case of $\omega_s = \omega_r$, there is a signal at 0 Hz and another one at $2\omega_s$ Hz. The latter, however, should be attenuated to an undetectable level by the low-pass filters shown in Figure 4.9. This way, both the unwanted signal appearing at double the frequency and all of the noise at different frequencies is attenuated.

Chapter 5

Technical design

This chapter discusses the implementation and integration of the various parts of the project. Even though the main focus here is on design and simulation, implementation is also covered where necessary.

5.1 Current driver

As was previously discussed, the existing driver does not need any hardware changes, but there are some notable details that play a role when configuring the driver.

5.1.1 Pulsing sequences

Previously, T_1 and **P-ODMR** were mentioned when discussing pulsed protocols. However, due to the high-frequency instability of the Analog Discovery signals, only sequences for T_1 measurements were made. Chapter 4.2.2 presented an overview of the T_1 pulsing scheme.

The lock-in amplifier reference signal can easily be generated by the Waveforms software. This is not the case for the laser driver signal. Waveforms supports custom sequence programming, however the system for writing these sequences only allows for pulses, which have a duration τ_{las} for which $\tau_{las} \geq \frac{T_{seq}}{100}$ holds true¹. It should also be noted that using the built-in pulse generation functionalities only allow for pulses that fit the formula $\tau_{las} = x \frac{T_{seq}}{100}$, where $x \in \mathbb{Z}^+$ and $x \leq 100$. These restrictions make it impossible for pulsing sequences to be designed in Waveforms. Thankfully, the software can read files, which makes it possible to customize a sequence more.

1	0	0	1	0
---	---	---	---	---

Figure 5.1: Example of a filled sequence buffer

But before delving into implementation details, the working of pulse generation in Waveforms needs to be discussed. An example of a filled Waveforms buffer, is shown Figure 5.1. A **TTL** signal can be generated using the values from it by setting the period T_{seq} of the sequence and the peak voltage V_{max} . Those two values are necessary, because the buffer contains normalized values. In the example, each element has a value of either 0 or 1, which translate to 0 or V_{max} when entered into the function generator. Furthermore, each pulse has a value of $\tau_{las} = \frac{T_{seq}}{5}$.

A MATLAB script (see Figure A.4 for full script) was written to generate buffer values based on the pulse duration τ_{las} , the scaling factor $\gamma = \frac{T_{seq}}{\tau_{las}}$ and the normalized dark time $t_d = \frac{\tau_d}{\tau_{las}0}$. Figure 5.2 shows a T_1 sequence where $\tau_{las} = 20$ μ s, $T_{seq} = 30$ ms and $\tau_d = 200$ μ s (consequently $\gamma = 1500$ and $t_d = 10$).

¹ T_{seq} is the period of the whole sequence

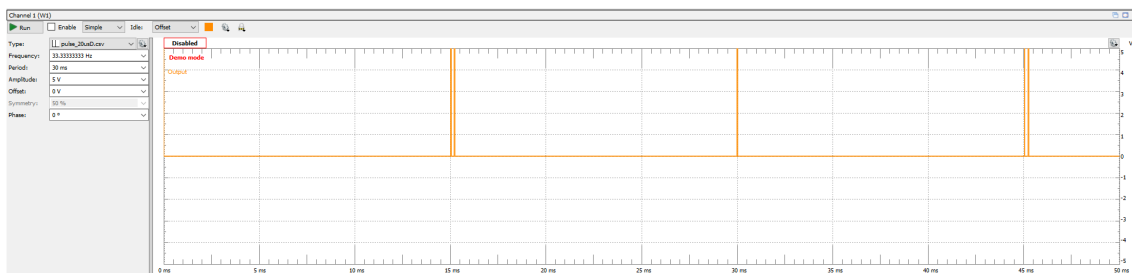


Figure 5.2: Waveforms function generator view after importing a T_1 pulse sequence

5.2 Photodetector design

As an integral part of the sensing setup, the photodetector needs a lot of attention. Good amplification is crucial to increasing the **SNR** of the quantum setup, however the materials used need to be accessible and cheap. Based on these considerations and the design ideas presented in the functional design (see Chapter 4.5.2), the photodetection circuit can be drawn up. The first three versions presented in this section of the report address the basic requirements of a **CW-ODMR** detector, which can have a bandwidth as low as 18 Hz [16]. In contrast, the fourth iteration of the photodetector design focuses mostly on providing an increase in bandwidth, which is necessary for pulsed protocols.

To summarize the circuit requirements, the input signal of the diode can range from 0 to 50 mA. This current needs to be amplified in the range from 0 to 5 V. In addition, the circuit should consider the quantum protocols that it will be used to detect. For **CW-ODMR**, low noise levels at low frequencies is desired and a bandwidth of 20 Hz is sufficient. In terms of pulsed protocols, T_1 is the main one that is considered. Based on the pulsing sequences shown in Sewani et al. [4], it was decided that the detector should be able to detect pulses of 5 μ s. Noise is harder to minimize with the broader bandwidth, which is why it was decided to have separate detectors for T_1 and **CW-ODMR**.

5.2.1 First iteration

As previously mentioned, the first iteration of the **PCB** uses component values provided by the client. Although its main purpose is to enable the setup to do **CW-ODMR** measurements, it also provides a reference for the following designs, which optimize the detector for the sensing setup and explore pulsing protocol support. In addition, the design was made so that the implementation price is as low as possible, at the request of the client.

There is no specific information for the design process, aside from the fact that the original designer made the photodetector for input currents in the range of 0 to 50 nA. Such low inputs require high R_1 values, however increasing the resistor value results in more biasing current going to the amplifier and a more limited dynamic range [17]. Furthermore, it is entirely possible that the original design did not thoroughly consider the bandwidth needed for different protocols, as **CW-ODMR** setups do not require broad bandwidths [16]. Biasing is another concern with this photodiode setup. The configuration shown in Figures 4.7 and 5.4 has the diode in the photovoltaic mode, which is suitable for low-frequency, low-light operation. In spite of this setup being suited to **CW-ODMR**, pulsed protocols require micro to nanosecond precision, which cannot be achieved with this version of the detector.

As some of the components used in the provided circuit can be used in later redesigns, it is important to discuss their most impactful parameters, which were used to determine if a certain component needed replacing.

Out of all of the components, the performance of the circuit is affected the most by the **TIA**-stage amplifier. This version of the photodetector uses an AD795 op-amp, which is suitable for low-frequency, low-noise applications like this one. Figure 5.3a shows the noise spectral density of the op-amp, which is low at low frequencies, but does not drop off much at higher frequencies. Another important consideration for the **TIA** op-amp is the supply current. At 5 V, the supply current is 1,5 mA. Lastly, the **Gain-Bandwidth Product (GBP)** of the AD795 is 1,6 MHz and the open-loop gain is 100 dB. These last two specifications are the most important for the frequency response of the whole circuit.

After the **TIA** op-amp, the post amplifier op-amp is the second most important component. In the photodetector, the non-inverting post-amplification stage is based on an AD820. Its noise

density is shown in Figure 5.3b. While it is significantly higher than the AD795, the AD820 has a much lower supply current of 0,8 mA.

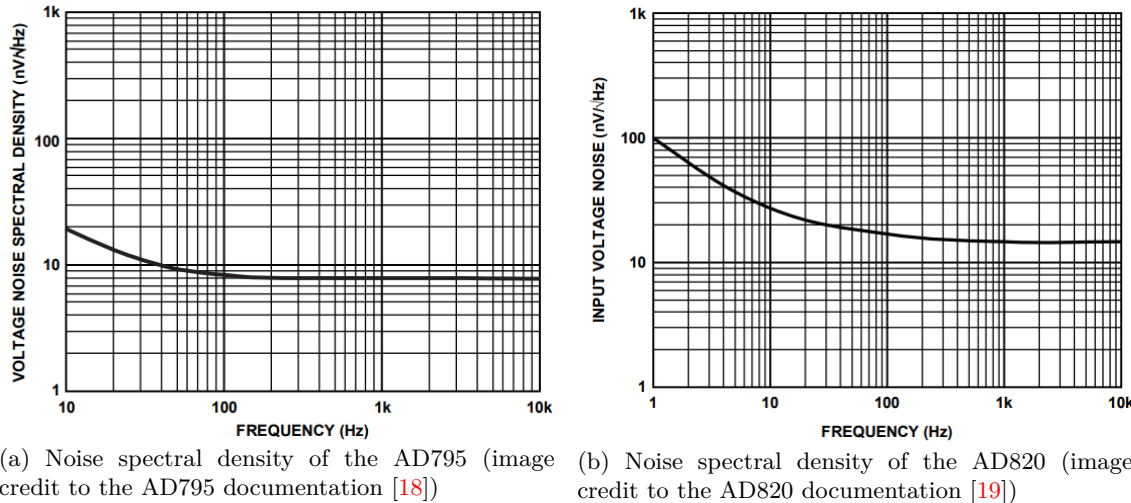


Figure 5.3: Noise spectral density of the amplifiers used in the pre and post-amplification stages of the photodetector

Lastly, the resistor values of the non-inverting amplifier feedback loop were also considered, although their impact on the signal is minimal. In the post-amplifier in Figure 4.8, the resistor R_3 affects the output noise the most [20, 21] and by reducing its value, the noise can be marginally decreased.

5.2.2 Second iteration

This photodetector iteration aims at redesigning the frequency response of the system for better stability. Due to time constraints, it uses the same topology as the first photodetector version.

That being said, it is still designed analytically, taking into account the general practices, but also considering more subtle factors that might hinder the performance of the system. This section uses the mathematical principles presented in [22–24] to optimize the design of the existing amplifier.

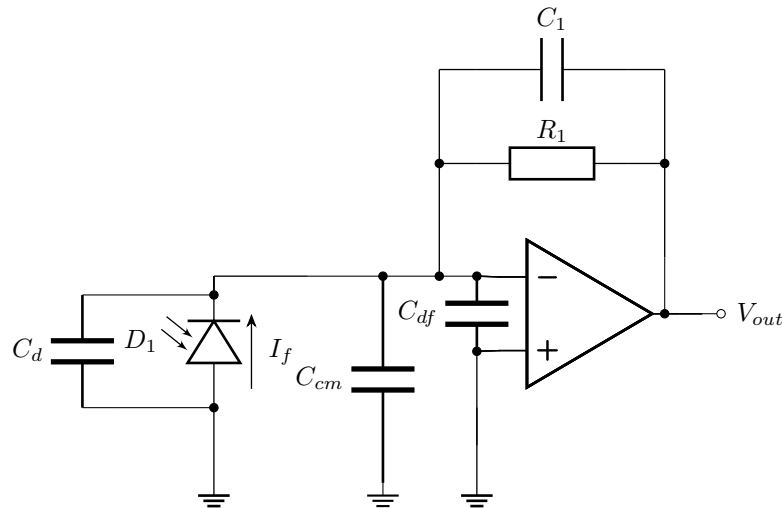


Figure 5.4: Parasitic capacitances in a TIA circuit

Introducing the real-world parasitic capacitances to the ideal TIA shown in Figure 4.7 results in the circuit in Figure 5.4. The diode capacitance C_d , combined with the differential and common-mode capacitances of the amplifier (C_{df} and C_{cm}), contributes a significant amount of capacitance to the circuit and can result in instability [25].

$$C_i = C_d + C_{df} + C_{cm} \quad (5.1)$$

The combined input capacitance (Equation (5.1)) is needed when solving the equation arising from **Kirchhoff's Current Law (KCL)** at the inverting input of the amplifier. Z_1 (Equation (5.2)), or the combined impedance of R_1 and C_1 , is another prerequisite for deriving the transimpedance Z_t using **KCL**. Additionally, the open-loop gain A_{ol} is needed for the derivation of the transimpedance. Equation (5.3) shows the open-loop gain, expressed with the **Direct Current (DC)** open-loop gain A_o and the open-loop cutoff frequency ω_o , which is equivalent to $\frac{v_{out}}{v_{in}}$.

$$Z_1(s) = \frac{1}{\frac{1}{R_1} + sC_1} \quad (5.2)$$

$$A_{ol}(s) = A_o \frac{\omega_0}{s + \omega_0} = \frac{v_{out}}{v_{in}} \quad (5.3)$$

Finally, the values in the **KCL** equation (Equation (5.4)) can be substituted, from which Z_t can be derived, as seen in Equation (5.5).

$$i_f = \frac{v_i}{\frac{1}{sC_i}} + \frac{v_{in} - v_{out}}{Z_1(s)} \quad (5.4)$$

$$Z_t(s) = \frac{v_{out}}{i_f} = (R_1 \frac{A_o}{1 + A_o}) \frac{\frac{\omega_o(1+A_o)}{(C_i+C_1)R_1}}{s^2 + s \frac{1+\omega_o(C_i+(1+A_o)C_1)R_1}{(C_i+C_1)R_1} + \frac{\omega_o(1+A_o)}{(C_i+C_1)R_1}} \quad (5.5)$$

Before moving on to the pole analysis, the impact of the quality factor Q on the system response should be considered (see Equation (5.13)). Two system poles present when $Q > 0, 5$. For $Q = \frac{\sqrt{3}}{3}$, the system has a Bessel response, which has the flattest group delay, however, if $Q = \frac{\sqrt{2}}{2}$, then the system has a Butterworth response, which means it has the flattest possible amplitude response. Although the group delay is not as important as the amplitude response, a Bessel response also results in smaller amount of overshoot and less jitter, which is why it is preferred. In the end, the choice between a Bessel and a Butterworth response only affects the circuit at high frequencies, which is not a concern when running **CW-ODMR** measurements. Still, it can be important when investigating photodetection for pulsed protocols.

$$H(s) = H_0 \frac{(-s_1)(-s_2)}{(s - s_1)(s - s_2)} = H_0 \frac{s_1 s_2}{s^2 + s(-s_1 - s_2) + s_1 s_2} \quad (5.6)$$

Based on this consideration, the poles can be found using the general form of a second order transfer function, shown in Equation (5.6). The general form also makes it obvious that the **DC** gain $H_0 \approx R_1$, assuming that A_0 is very big.

$$\begin{cases} -s_1 - s_2 = \frac{1+\omega_o(C_i+(1+A_o)C_1)R_1}{(C_i+C_1)R_1} \\ s_1 s_2 = \frac{\omega_o(1+A_o)}{(C_i+C_1)R_1} \end{cases} \quad (5.7)$$

Taking the general-equation poles and their counterparts from the Z_t expression yields the system of equations shown in Equation (5.7). Solving it results in a quadratic equation with roots shown in Equation (5.8).

$$s_{1,2} = -\frac{1 + \omega_o(C_i(1 + A_o)C_1)R_1}{2(C_i + C_1)R_1} \left(1 \pm j \sqrt{\frac{4\omega_o(1 + A_o)(C_i + C_1)R_1}{(1 + \omega_o(C_i + (1 + A_o)C_1)R_1)^2} - 1} \right) \quad (5.8)$$

$$s_{1,2} = -\frac{3}{2}(1 \pm j \frac{\sqrt{3}}{3}) \quad (5.9)$$

Achieving the desired system, can be done by getting the roots of the general form of a Bessel filter (as seen in Equation (5.9)) and using the imaginary parts to get Equation (5.10). From it, a the quadratic equation in Equation 5.11 can be derived. This expression can be solved with the quadratic formula again, finally resulting in an answer for the compensating capacitor C_1 .

$$\frac{4\omega_o(1 + A_o)(C_i + C_1)R_1}{(1 + \omega_o(C_i + (1 + A_o)C_1)R_1)^2} = \frac{4}{3} \quad (5.10)$$

$$C_1^2(R_1(1 + A_o))^2 + C_1\omega_o(1 - C_i)((1 + A_o)R_1) - 3\omega_o(1 + A_o)C_iR_1 + C_i^2 + 2C_i + 1 = 0 \quad (5.11)$$

$$C_1 = \frac{-2\omega_o R_1 C_i \pm \sqrt{12A_o C_i R_1 \omega_o - 3}}{2\omega_o R_1 (1 + A_o)} \quad (5.12)$$

Although the quadratic formula in Equation (5.12) says there are two solutions for the capacitor, the term under the square root will always be much bigger than the rest of the numerator², effectively determining the sign of the roots. Simply put, this leaves only one root possible, as capacitors cannot have negative capacitance values.

To further characterize the system, the cutoff frequency ω_c and damping factor Q can be calculated, because the system adheres to the general form, shown in Equation (5.13). Substituting in the pole expressions from Equations (5.6) and (5.7).

$$H(s) = H_o \cdot \frac{\omega_c^2}{s^2 + s \frac{\omega_c}{Q} + \omega_c^2} \quad (5.13)$$

$$\begin{cases} \omega_c = \sqrt{\frac{\omega_o(1+A_o)}{(C_i+C_1)R_1}} \\ Q = \omega_c \frac{(C_i+C_1)R_1}{1+\omega_o(C_i+(1+A_o)C_1)R_1} \end{cases} \quad (5.14)$$

In the process of designing the TIA circuit, the noise should be considered. Figure 5.5 shows the thermal noise generated by the resistor (modeled as the current source i_{nR}) and the differential noise of the amplifier (modeled as the current source i_{nA})³.

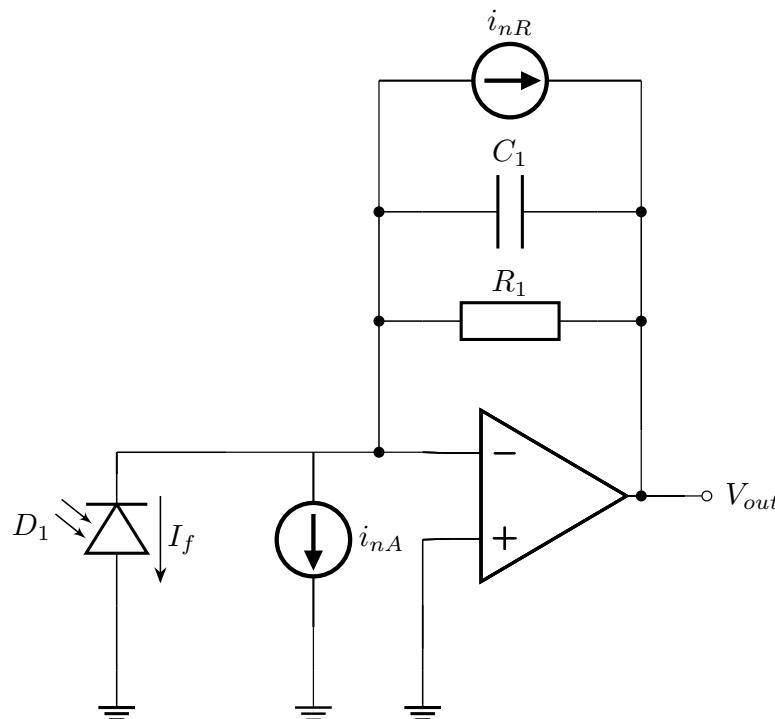


Figure 5.5: Noise current sources in a TIA circuit

Calculating i_{nR} can be done using the Johnson-Nyquist formula, as shown in Equation (5.15). Given the fact that the temperature T and noise cutoff frequency δf cannot be modified in this case, R_1 is the only variable that can be used to lower the thermal noise current.

$$i_{nR} = \sqrt{\frac{4kT\Delta f}{R_1}} \quad (5.15)$$

Combining the noise sources leads to Equation (5.16), which also shows that the noise can be modeled as voltage sources.

$$i_n(f) = \sqrt{i_{nR}^2 + i_{nA}^2} \Leftrightarrow v_n(f) = \sqrt{v_{nR}^2 + v_{nA}^2} \quad (5.16)$$

²Assuming real-world amplifier and diode specifications, and realistic transimpedance gain requirements

³Other noise generators, like the gate shot noise, channel noise and induced gate noise can also be calculated, but because they largely depend on the underlying technology of the Field-Effect Transistor (FET) op amp, they have not been investigated

The noise gain is the ratio of the output noise and the input noise. This ratio gives a better understanding of what frequencies of noise are the most problematic if they appear at the input of the **TIA**. In order to get a better understanding of the noise gain, its transfer function can be calculated in much the same way as the transimpedance (Equations 5.3 - 5.5), leading to Equation (5.17). The transfer function shown in it can be broken down into two components: a low-pass and a band-pass component. In the numerator expression $sA_o\omega_o$ contributes the band-pass component and the expression $\frac{A_o\omega_o}{(C_i+C_1)R_1}$ is responsible for the low-pass component. Figure 5.6 shows an example of the frequency response of the noise transfer function.

$$H_n(s) = \frac{v_o}{v_n} = \frac{A_o\omega_o(s + \frac{1}{(C_i+C_1)R_1})}{s^2 + s(\frac{1}{(C_i+C_1)R_1} + \omega_o(1 + A_o \frac{C_1}{C_i+C_1})) + \frac{\omega_o(1+A_o)}{(C_i+C_1)R_1}} \quad (5.17)$$

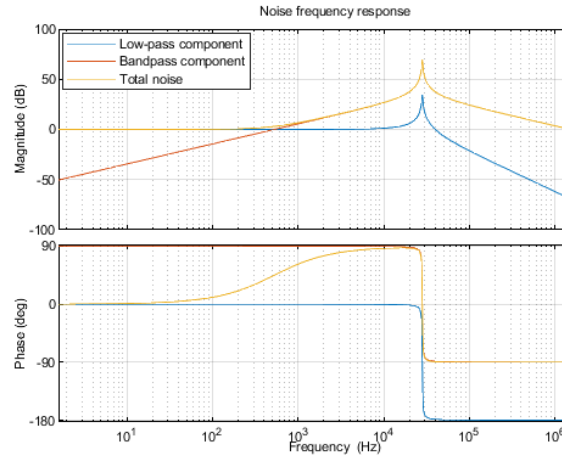


Figure 5.6: Plot of the components of the noise and the total noise

While it might not be immediately obvious from the mathematical expression, the noise gain is 0 dB at low frequencies, but it peaks when $f \approx f_c$.

Firstly, the low-frequency response of the system can most easily be demonstrated by calculating it at a frequency $\omega = 0 \text{ rad s}^{-1}$. This gives us the **DC** gain shown in Equation (5.18), which is close to 1 for real amplifiers, in which the gain is finite.

$$H_n(0) = \frac{\frac{A_o\omega_o}{(C_i+C_1)R_1}}{\frac{\omega_o(1+A_o)}{(C_i+C_1)R_1}} = \frac{A_o}{A_o + 1} \quad (5.18)$$

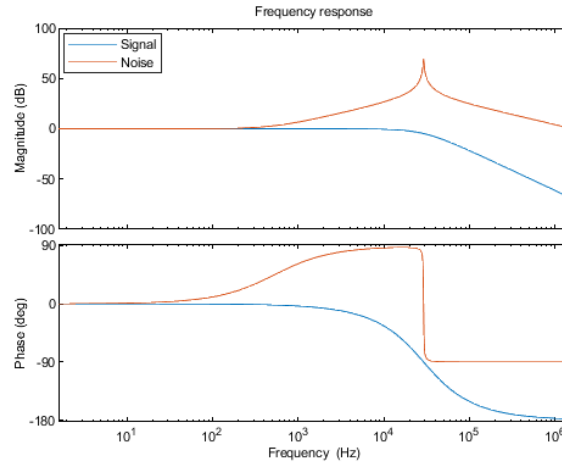


Figure 5.7: Comparison between the noise frequency response and the normalized signal frequency response

Secondly, the peak is caused by the combination of both components. The center frequency of the band-pass component corresponds to the cutoff frequency of the low-pass, which makes the gain at that frequency the highest. What is more, the peak-gain frequency of the noise matches the signal transfer function cutoff, which can be seen in Figure 5.7.

5.2.3 Third iteration

While the second version of the photodetector focuses on improving the TIA performance, the third iteration is more about adapting the design for the setup. In particular, this iteration tries to simplify the power delivery and optimize the size of the design, while keeping the amplifying circuit unchanged. In spite of the added power management, this version of the system is made so that it still costs around the same as the previous ones.

The most important considerations for the setup are function and size. Form factor constraints arise from the fact that the setup needs to be as small and adhere to the Thorlabs mounting standard. Photodetection also needs to not require many external connections or ideally be standalone. This is feasible for the data flow, as the photodetection PCB only needs light and an output to work. Unlike the data connections, version two of the design has a suboptimal power delivery system, as it uses three pins for the supply of power.

Three alternatives methods for power delivery were considered, all of which only need power and ground to work. The first one is an onboard split-rail power supply, which would take the power input and would output a fixed positive and negative voltage. Figure 5.8 shows an example of what a split-rail supply implementation might look like. There are also external option [26], which might be necessary in the future, if the setup size needs to be reduced even more.

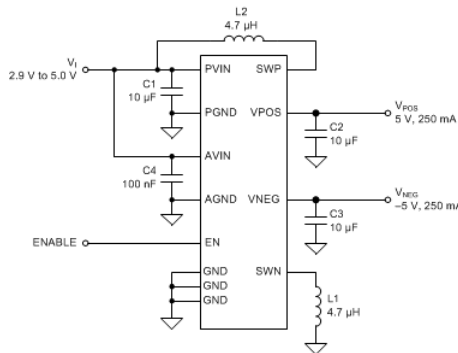


Figure 5.8: Example of a split-rail power supply implementation using the TPS65133 IC (image credit to [27])

A simpler solution would be to use a virtual ground driver IC, as it would provide a reference point at half of the supply voltage. Such a supply would also be good for decreasing the size, as the PCB needs minimal additions to satisfy the power needs of the photodetector. Additionally, a virtual ground circuit, which behaves similarly, can be made using two voltage regulators. The example in Figure 5.9 is a slightly more stable implementation

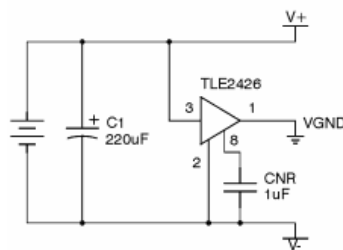


Figure 5.9: Example of a virtual ground driver using the TLE2426 IC (image credit to [28])

Another possibility is to implement a charge pump (see Figure 5.10), which inverts the input voltage. This setup would only need half of the input voltage required for the virtual ground solution, effectively enabling it to be powered via a standard Universal Serial Bus (USB) connector.

The specifications of the different power supply solutions are shown in Table 5.1, from which can be deduced that there is a correlation between complexity and performance. The split-rail power

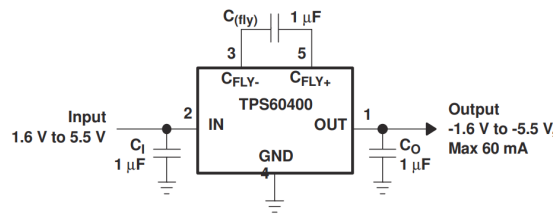


Figure 5.10: Example of a charge pump inverter using a TPS6040x family IC (image credit to [29])

	Split-rail power supply	Virtual ground	Charge pump
IC	TPS65133	TLE2426	TPS60400
V_{in} (V)	5	10	5
V_{out} (V)	± 5	± 5	-5
I_{out} (mA)	250	40	60
Current draw (μA)	15	300	210

Table 5.1: Comparison of power supply options

supply, as the most complex solution, has the biggest current output range and lowest current consumption, but as illustrated in Figure 5.8, there are a number of other components that are required for proper implementation. In contrast, the virtual ground supply concept has relatively poor specifications compared to the other options, but it is the only solution that does not employ a switching mechanism, thus avoiding any possible noise. Lastly, the charge pump inverter offers reasonable performance, while not needing as many extra components as the split-rail supply. Furthermore, it addresses the stability concerns that might arise when using a virtual ground IC.

Ultimately, the charge pump is the most fit for this project, because it is relatively simple, while also offering excellent stability. The decision was reached only after taking into account the power calculations from Chapter 4.5.3, according to which all devices can handle the power requirements of the circuit. Another important factor when making the decision was the efficiency of the switching solutions. Based on slight fluctuations in the amount of current drawn, the charge pump can have as much as twice the efficiency of the split-rail power supply [27, 29], due to its high efficiency at low currents.

The design in Figure 5.10 is recommended by the manufacturer. Unlike the flying capacitor C_{fly} , which does not affect the behavior of the IC, both the input C_I and output C_O capacitors have to be chosen carefully. Too low of an input or output capacitance can cause an unwanted ripple. What is more, the **Equivalent Series Resistance (ESR)** of C_O also has a significant effect on the output ripple, as is evident from Equation (5.19) [29]. In it, I_O is the output current and f_{osc} is the switching frequency of the pump.

$$V_{Or} = \frac{I_O}{f_{osc} C_O} + 2I_O(ESR_{CO}) \quad (5.19)$$

5.2.4 Fourth iteration

Although the previous iterations provided a cheap and reliable photodetector for CW-ODMR, the narrow bandwidth prevents them from measuring pulsed protocols. This iteration is specifically designed for T_1 measurement support. Although it is somewhat more expensive than the previous iteration, version four justifies the price by offering significant sensing performance gains.

The simplest way to increase the bandwidth of the TIA is to decrease its transimpedance gain. Additionally, an op-amp with a higher GBP will also contribute to a substantial increase in gain. Figure 5.11 shows the ideal version of the TIA, used in the second and third iteration of the system (in blue). It uses an AD795 amplifier, which has a 1,6 MHz GBP. The resulting cutoff frequency is 19,69 kHz. Only swapping the AD795 for an ADA4637, which has a 79 MHz GBP, results in the system response in orange. Its cutoff frequency is 138,87 kHz. Both lines show a system with the same transimpedance gain and consequently R_1 value. On the other hand, the yellow line shows the increase in bandwidth with a 10 times smaller gain⁴. The ADA4637 system with 1 MΩ R_1 has a cutoff frequency of 437,32 kHz.

⁴The plot shows normalized gain of each system, which is why the first two systems (140 dB) have the same gain as the last system (120 dB)

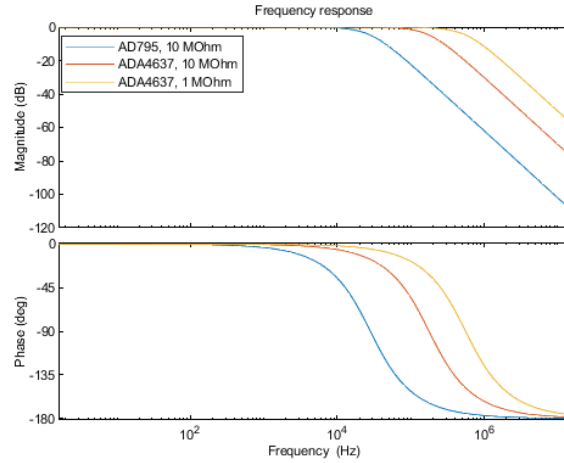


Figure 5.11: Bandwidth comparison of the third iteration of the TIA (based on AD795) and one based on an ADA4637 op-amp with a $10\text{ M}\Omega$ and a $1\text{ M}\Omega$ R_1

While these changes contribute to an improved bandwidth, they are limited by the compensation capacitor C_1 . Its purpose is to counteract the negative effects of the diode capacitance C_d and stabilize the frequency response of the system. In doing so, however, it also reduces the bandwidth of the system. Decreasing the capacitance of C_1 outright can lead to unwanted resonance, but it is possible to stabilize C_d and consequently reduce the value of C_1 by using bootstrapping. The design discussed in this section is based on [23, 30–32].

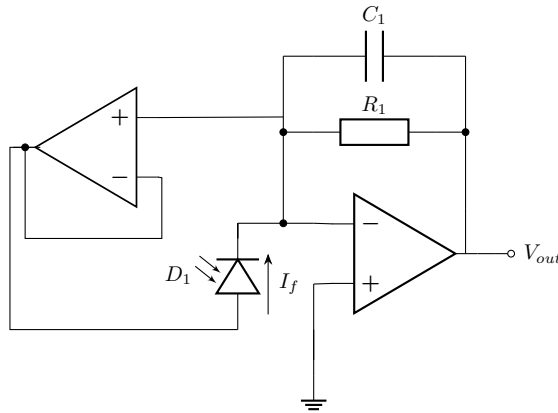


Figure 5.12: Shunt bootstrap TIA circuit

Figure 5.12 shows the bootstrapped TIA. The same analysis as in Chapter 5.2.2 can be applied to the circuit, which leads to the transimpedance Z_t in Equation (5.20). The additional op-amp buffer creates an extra pole and zero. In the expression, C_i is the sum of the common-mode and differential capacitance of the amplifier, C_d is the photodiode capacitance, A_o is the intrinsic open-loop gain of the amplifier, ω_o is the open-loop cutoff frequency and all other parameters correspond to the ones in Figure 5.12.

$$Z_t(s) = \frac{v_{out}}{i_f} = \frac{R_1}{s^2 \frac{(C_i + C_1 + C_d)R_1}{\omega_o A_o} + s \left(\frac{(C_i + C_1 + C_d)R_1}{A_o} + C_1 R_1 + \frac{1}{\omega_o A_o} \right) - \frac{s(s + \omega_o)C_d R_1}{s + \omega_o(1 + A_o)} + \frac{A_o + 1}{A_o}} \quad (5.20)$$

Determining the ideal C_1 by solving the characteristic equation of the system analytically is even harder than in the previous designs, which is why the system equation was solved by trial and error, and with the use of MATLAB to plot the system response with different capacitor values. The solution is discussed in more detail in Chapter 5.3.4.

While the improvements to the TIA are crucial for broadening its bandwidth, the changes also affect the post-amplification stage. It needs to compensate for the gain reduction that was previously discussed. Despite, a simple gain increase being a viable solution, this will also reduce

the bandwidth. Similarly to the **TIA**, the non-inverting amplifier is also affected by the gain-bandwidth relationship, as dictated by the **GBP**, shown in Equation (5.21), where A_v is the gain of the stage.

$$f_c = \frac{GBP}{A_v} \quad (5.21)$$

An alternative to increasing the gain is to add a second non-inverting stage with the same gain. By doing this, the bandwidth does not decrease as a result of the gain-bandwidth relationship, but the cutoff frequency $f_{c\alpha}$ of single-stage non-inverting amplifier even increases as shown in Equation (5.22)⁵ [33]. In the equation, A_{df} is the bandwidth increase due to the single-stage gain reduction.

$$f_c \approx A_{df} \left(\frac{1}{f_{c\alpha}^2} + \frac{1}{f_{c\alpha}^2} \right)^{-\frac{1}{2}} = \frac{A_{df}}{\sqrt{2}} f_{c\alpha} \quad (5.22)$$

It should also be noted that the equivalent resistance of the gain-setting resistors, combined with the parasitic capacitances of the op-amp, create a zero, the impact of which can be reduced by decreasing the value of the resistors. This can be observed from the relationship of the resistance to the phase margin, as seen in Equation (5.23). In it, resistors R_2 and R_3 correspond to the ones in Figure 4.8. C_{cm} and C_{df} denote the common-mode and differential capacitance of the op-amp.

$$\frac{1}{2\pi (C_{cm} + C_{df}) \frac{R_2 R_3}{R_2 + R_3}} > \frac{GBP}{1 + \frac{R_3}{R_2}} \quad (5.23)$$

It is possible to simplify the formula, because when designing the amplifier, the ratio of the resistors is fixed ($R_3 = A_r R_2$, where A_r is the resistor ratio). Solving for R_2 then gives Equation 5.24.

$$R_2 < \frac{(1 + A_r)^2}{2\pi A_r (C_{cm} + C_{df}) GBP} \quad (5.24)$$

Finally, Figure 5.13 shows the schematic of the system after all the modifications. Because of noise concerns, the resistor values were reduced significantly, which, as previously mentioned, contributes to lower noise in the post-amplification stage.

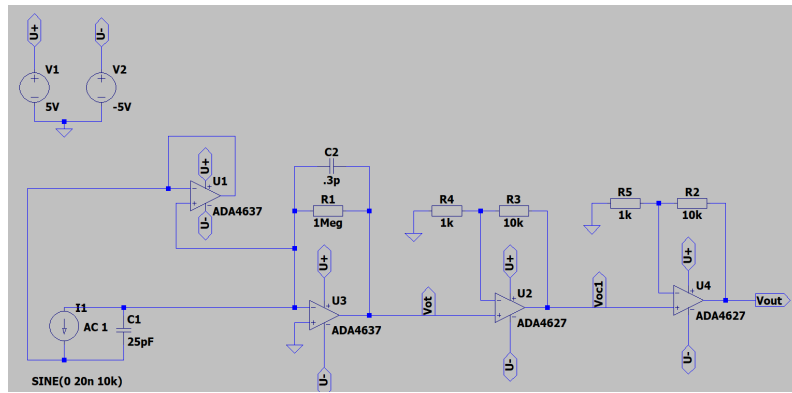


Figure 5.13: Schematic of the fourth iteration of the **TIA**

5.2.5 Final CW-ODMR iteration

At the beginning of the project, the client wanted an all-encompassing solution for the detection of all protocols. Although this is possible, as is clear from the photodetectors on the market, such a solution can cost in the range of hundreds to thousands of euros. Bringing costs down is important for the client, which is why it was decided to have separate photodetectors for **CW-ODMR** and for **P-ODMR**.

Detecting **CW-ODMR** is possible with a much lower bandwidth than pulsed protocols, which removes the need for post amplification and thus brings down the overall noise of the system, as well as its noise susceptibility. This is good, because the client is interested in having a portable **CW-ODMR** demonstrator and reducing noise susceptibility in such a noisy environment is crucial. In

⁵The formula assumes the non-inverting stages have the same parameters and use the same components as in the actual design

the end, the design of this system seeks to minimize noise as much as possible, without necessarily considering the bandwidth.

As the second iteration of the photodetector has a serviceable design, the final version of the photodetector is based on it. The first and most important change for reducing the overall noise of the system is the removal of the non-inverting stage, which necessarily results in an increase of the transimpedance gain. Removing the post amplifier contributes most of the noise reduction, but the transimpedance gain increase, which is equivalent to the value of the gain-setting resistor of the **TIA**, also reduces its thermal noise, according to Formula (5.15).

Furthermore, significant noise reduction can be brought about by making changes to the **TIA**. The op-amp choice is the most impactful of all. The OPA827 was chosen, due to its excellent noise characteristics. Other alternatives, like the OPA1656, AD743 and ADA4627 were briefly considered, because of their good noise characteristics, but their low-frequency spectral noise density is higher than the OPA827.⁶. In addition, the LT1128 was also explored as a possible alternative. However, it has a significantly higher input bias current⁷, which will affect the photoconductive-mode diode and thus substantially increase its noise. Lower input bias current is the reason why the ADA4627 is the best alternative to the OPA827, despite its somewhat worse noise characteristics.

Finally, the compensation capacitor of the **TIA** can also be adjusted to reduce unwanted noise. Figure 5.14 shows the model of the voltage gain of the noise when the compensation capacitor is set so that the system has a Bessel response. The large spike created by the band-pass component can be filtered out by increasing the capacitance, thus substantially reducing the high-frequency noise of the system. For the final design, various standardized values of increasing capacitance were tested with simulation software, until a fitting value was found.

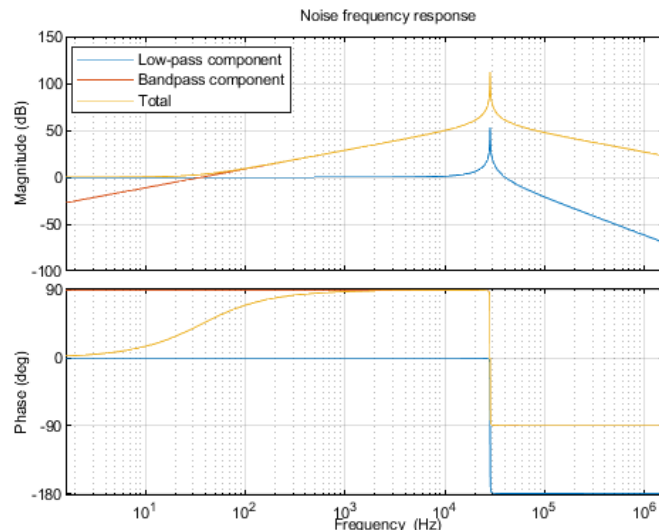


Figure 5.14: Theoretical noise model of an OPA827-based **TIA** with a Bessel response

After implementing all the aforementioned changes, the final version of the **CW-ODMR**

5.3 Photodetection simulation

Simulation is an important part of the designing process, as digital models of devices can be more detailed than the mathematical models presented thus far. Using different simulation programs, the real-world performance can be approximated and the math can be validated.

5.3.1 First iteration

Figure 5.15 shows the schematic of the circuit. The capacitor C_4 , as well as the current source I_1 are used to simulate the behavior of a photodiode.

⁶ADA4627: 4,8 nV Hz^{-0,5} at 10 kHz, but 16,5 nV Hz^{-0,5} at 10 Hz; OPA1656: 2,9 nV Hz^{-0,5} at 10 kHz, but 37 nV Hz^{-0,5} at 10 Hz; AD743: 2,9 nV Hz^{-0,5} at 10 kHz, but 22 nV Hz^{-0,5} at 1 Hz; OPA827: 3,8 nV Hz^{-0,5} at 10 kHz and 7,1 nV Hz^{-0,5} at 10 Hz

⁷25 nA compared to the 10 pA of the OPA827

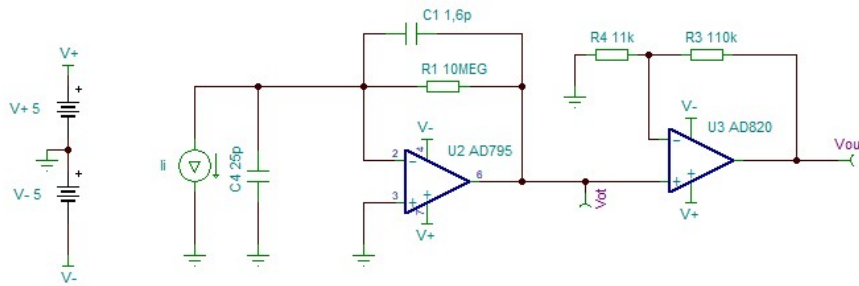


Figure 5.15: First iteration of the photodetector circuit

Tina-TI was used to simulate and visualize the DC gain and frequency response of the system, as seen in Figure 5.16. The signals V_{ot} and V_{out} correspond to the output of the transimpedance and non-inverting amplification stage respectively. The AC plot (Figure 5.16a) shows the cutoff, at 10,77 kHz, and the gain inside the gain bandwidth, which is 160,82 dB. The DC plot (Figure 5.16b) shows the voltage with respect to the current and demonstrates the linearity of the system in the range of 0 to 46,31 nA. After V_{out} reaches 5 V, the output remains fixed, because it cannot exceed the voltage provided to the amplifier.

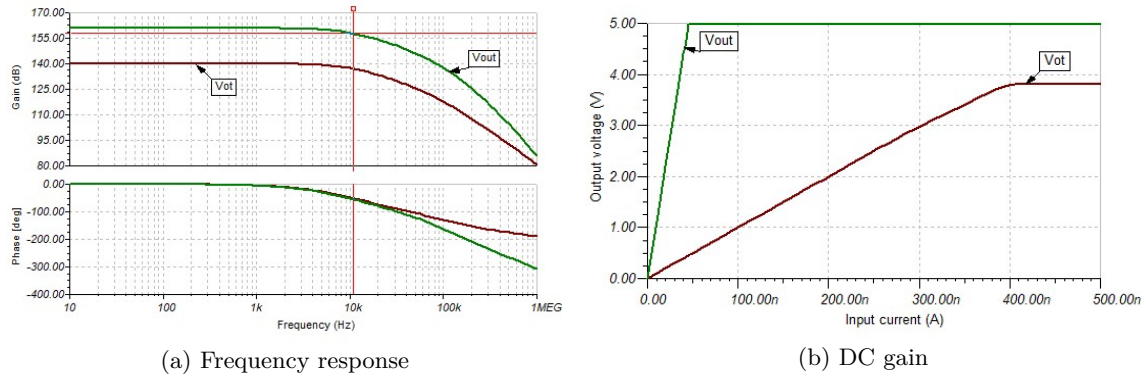


Figure 5.16: Simulation of the first iteration of the photodetector

5.3.2 Second iteration

A MATLAB script was written to calculate the component values based on the calculations in Chapter 5.2.2.

MATLAB calculates the component values with high precision and sourcing components with the exact values is not feasible, which is why components with standard values will be used in the setup. Simulations with standardized components were also done to compare the mathematically-ideal setup to the one in practice.

TIA version	v2 (Ideal)	v2 (Real.)	v1
C_1 (pF)	0,969 04	1	1,6
f_c (kHz)	22,0768	21,167	11,2422
Q	0,577 35	0,559 96	0,354 87

Table 5.2: TIA parameters with a 10 MΩ feedback resistor R_1

Table 5.2 contains the MATLAB calculation results and shows the values of f_c and Q when only C_1 changes. R_1 is kept the same, as it is equivalent the DC transimpedance Z_{tDC} ⁸. Importantly, the results show that the previous iteration had an overdamped response. Although the quality factor with realistic component values is also lower than the ideal $Q = \frac{\sqrt{3}}{3}$, the system still behaves approximately like a Bessel filter.

⁸For realistic op-amps, $\frac{A_o}{A_o + 1} \rightarrow 1$, which means $Z_{tDC} \equiv R_1$ can be assumed to simplify explanations

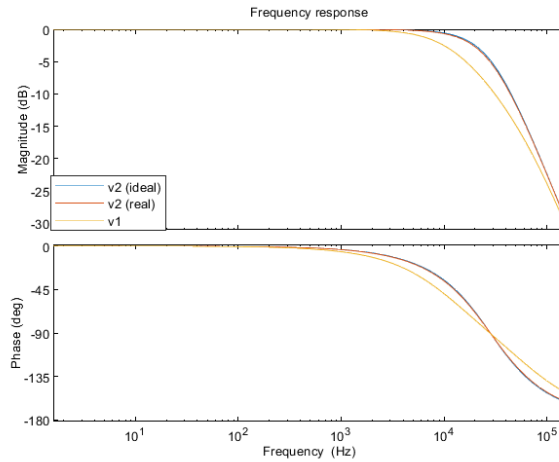


Figure 5.17: Bode plot of the system with different capacitors

Using these values, the system model was calculated and plotted in Figure 5.17. Certain differences can be seen between the two iterations. Most notably, the cutoff frequency f_c of the first iteration is somewhat smaller than that of the second iteration. Furthermore, it can be observed that both the ideal and realistic versions of the system behave similarly.

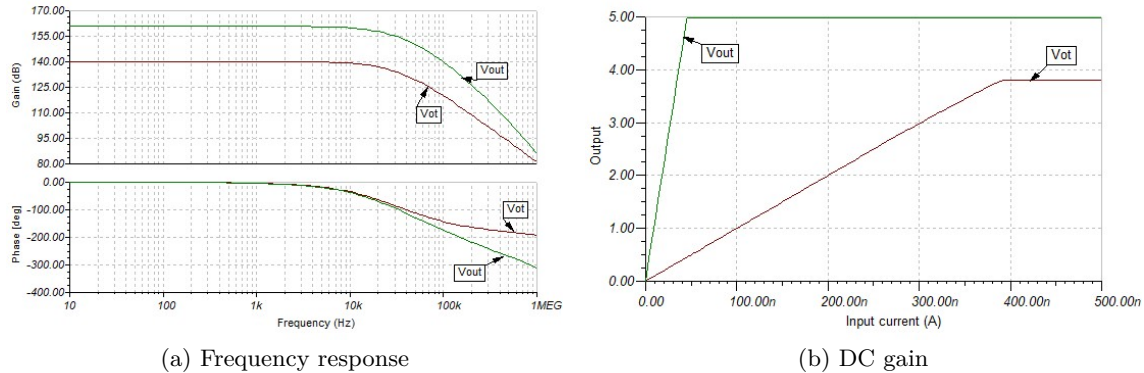


Figure 5.18: Simulation of the second iteration of the photodetector

Figure 5.18 confirms the calculations, with some slight differences that can be attributed to the [Simulation Program with Integrated Circuit Emphasis \(SPICE\)](#) models. As predicted, the frequency response of the circuit shows an increased cutoff frequency of 19,69 kHz, 8,92 kHz more than the previous iteration. Up to the cutoff frequency, the transimpedance gain is 160,83 dB, which is almost the same as the former gain of 160,82 dB. Furthermore, Figure 5.18b shows that, similarly to the first iteration, the system displays linearity in the range of 0 to 45,86 nA. This is a reduction of 450 pA compared to the previous version and also 4,14 nA less than the ideal upper limit of the linear region.

Additionally, a MATLAB script was used to calculate the [TIA](#) noise transfer function, the output of which is shown in Figure 5.19. As discussed in Chapter 5.2.2, the noise gain spikes at the cutoff of the signal transfer function.

5.3.3 Third iteration

Before deciding on a power supply system, the power requirements needed to be compared to the specifications listed in Table 5.1. A MATLAB script, which can be found in Appendix A, was written and used to calculate that, given a ± 5 V supply, the system requires 2,3021 mA of current. All solutions can provide that amount of current with reasonable overhead, which is why the choice was based on size, complexity and stability.

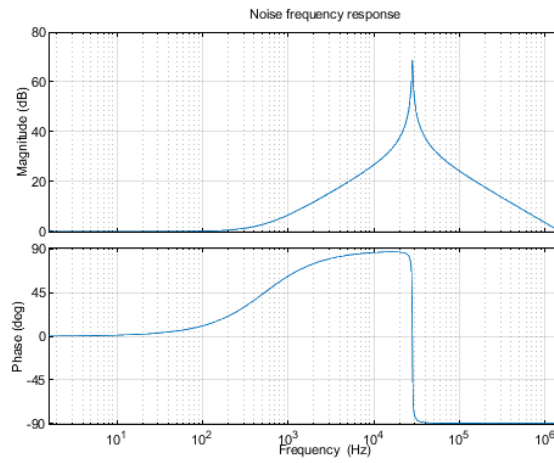


Figure 5.19: Noise transfer function of the **TIA** using an AD795, 10 M Ω resistor and an ideal compensating capacitor

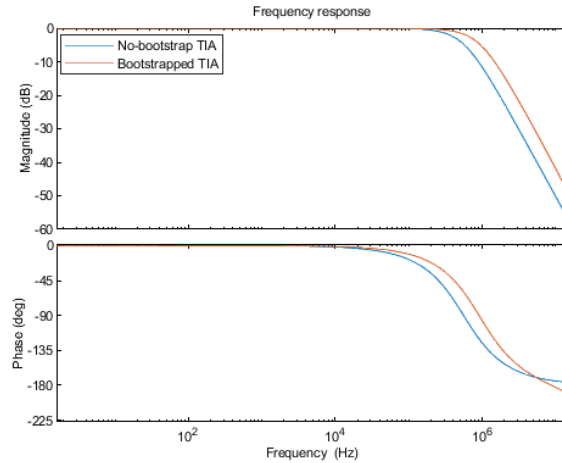


Figure 5.20: Comparison of a bootstrapped **TIA** and a **TIA** with only a compensating capacitor, both with the same transimpedance gain

5.3.4 Fourth iteration

As previously discussed, the value of the capacitor could not be determined analytically, however an approximate value was calculated using MATLAB simulations. Figure 5.20 shows that the bootstrapped system demonstrates a significantly increased bandwidth. According to Table 5.3, the bootstrapped amplifier still has a quality factor Q close to the ideal 0,577 35, which is even better than the previous iterations of the system. Furthermore, the capacitor value is standard, meaning that the value can be used in the physical system without further approximations.

TIA version	v4 (Bootstrapped)	v4 (No bootstrap)	v2/v3
C_1 (pF)	0,3	0,492 65	1
R_1 (M Ω)	1	1	10
f_c (kHz)	724,69	437,32	21,167
Q	0,578 14	0,577 35	0,559 96

Table 5.3: Comparison of **TIA** parameters of the fourth and second/third iteration of the system

Additionally, the post-amplification part of the system was simulated with and without the cascaded stages. Shown in Figure 5.21, the results demonstrate a significant increase in bandwidth. The plot of the bootstrapped **TIA** discussed in the design section (Chapter 5.2.4) with a single 40 dB non-inverting stage shows a flat response with a cutoff frequency of approximately 194,45

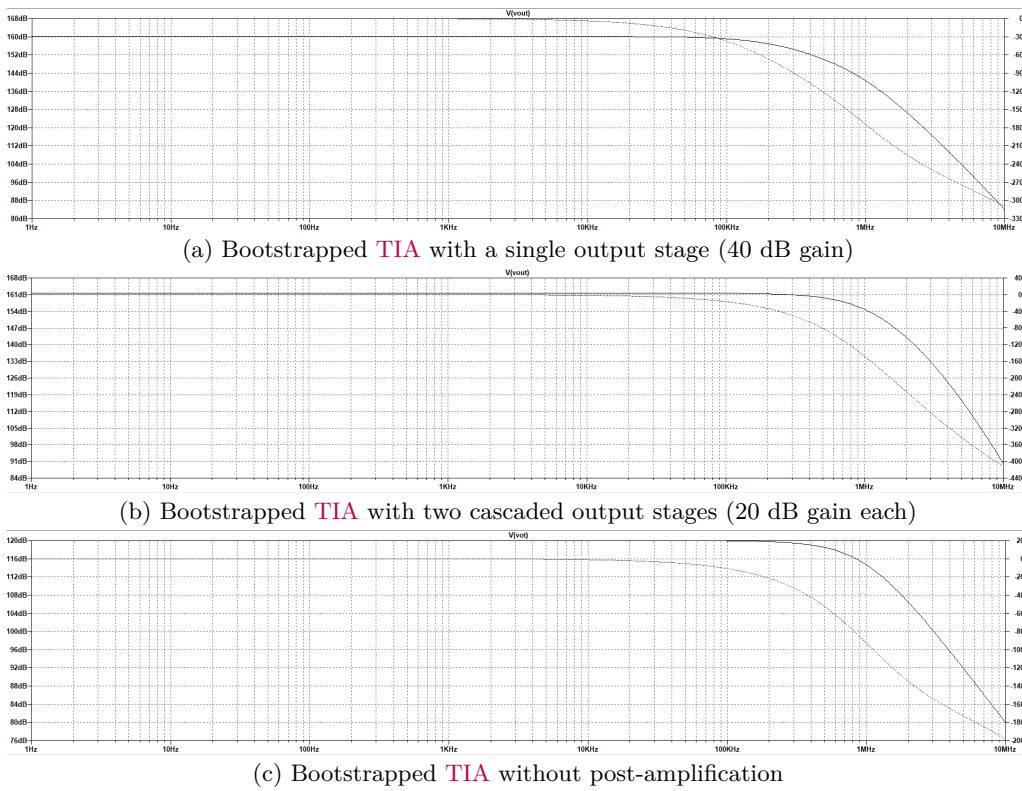


Figure 5.21: Simulation of the effect of cascading on the bandwidth of the fourth iteration of the photodetector

kHz. This is significantly lower than 716,67 kHz, which is the bandwidth of the TIA without any post-amplification (Figure 5.21c). Figure 5.21b shows the increased bandwidth of 638,08 MHz when two stages are used instead of one. In spite of the significantly bigger cutoff frequency, the response is not maximally flat, which means the linearity at high frequencies is subpar.

Here it is important to mention that while cascading increases the bandwidth of the system, it also results in more noise. Figure 5.22 shows the effect of cascading. Aside from the obvious increase around the cutoff frequency, the noise at 1 Hz also increases from $14,5 \text{ nV Hz}^{-0,5}$ to $18 \text{ nV Hz}^{-0,5}$.

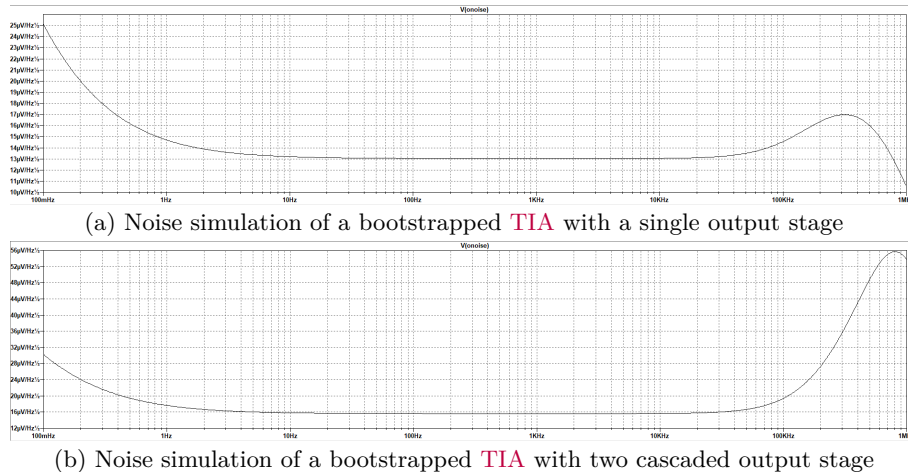


Figure 5.22: Simulation of the effect of cascading on the noise of the fourth iteration of the photodetector

5.3.5 Final CW-ODMR iteration

After implementing all the changes, the final version of the CW-ODMR, the simulation circuit in Figure 5.23 was used to verify the noise improvements. Additionally, the same circuit was tested

with the ADA4627, because in the initial design stage it was seen as the second most promising op-amp.

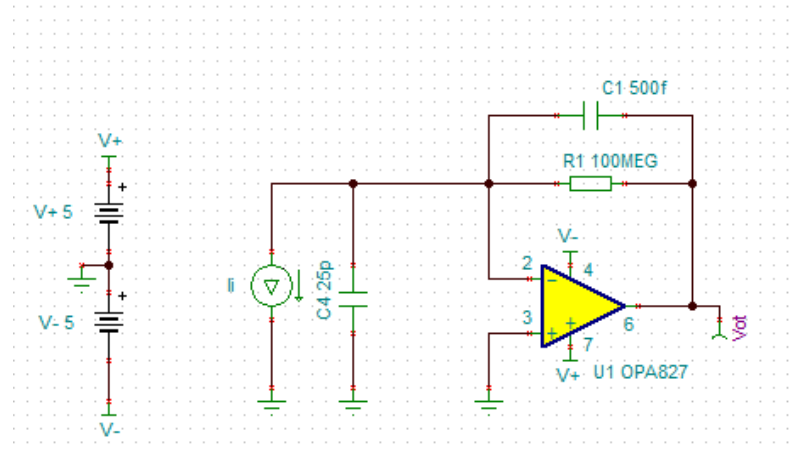


Figure 5.23: Circuit used for the simulation of the CW-ODMR photodetector

Figure 5.24 shows a comparison of the noise of the OPA827-based TIA with the alternative ADA4627-based TIA. The results show the OPA827 has marginally better noise performance at higher frequency. However, it also performs marginally worse at lower frequencies.

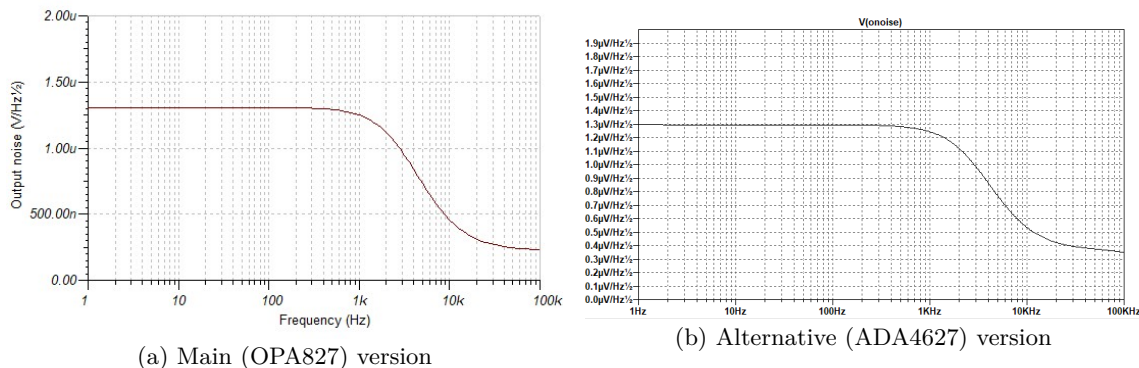


Figure 5.24: Simulation of the noise of the photodetector with different op-amps

In addition, the two possible implementations of the CW-ODMR photodetector were compared to the simulations of the second iteration. Table 5.4 shows both new versions demonstrate major noise improvements over the old one in the whole frequency range.

	v2	v5	Alternative v5
IC	AD795	OPA827	ADA4627
Bandwidth (kHz)	21,167	3,2	3,2
Noise at 1 Hz ($\mu\text{V}\text{Hz}^{-0.5}$)	4,63	1,31	1,30
Noise at 100 kHz ($\text{nV}\text{Hz}^{-0.5}$)	1830	230,41	347,87

Table 5.4: Comparison of the final CW-ODMR photodetector with its alternatives

5.4 Photodetection implementation

Creating the physical PCB is a more straightforward process than the design and simulation, but it still needs to be discussed. Aside from the boards, this section also covers the essential components.

5.4.1 First iteration

Figure 5.25 shows the back side of the PCB. It hosts all components, except for the photodiode, which sits unobstructed on the front side. Requirements for the physical dimensions were also set

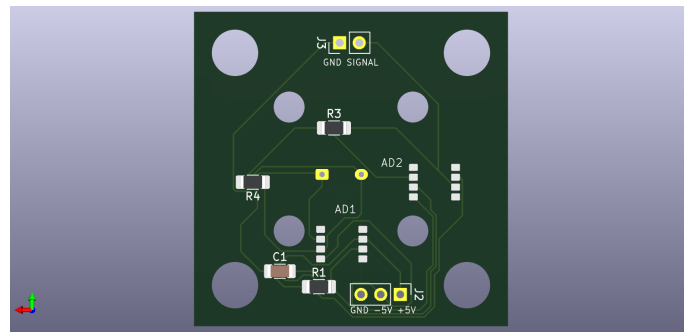


Figure 5.25: First iteration of the photodetection PCB

by the client. The **PCB** needs to fit the Thorlabs mount standard, since the rest of the setup also uses it. For photodetection, the system uses a BPW34 through-hole diode. Additionally, the **TIA** uses an AD795 op-amp and the post-amplifier uses an AD820.

5.4.2 Second iteration

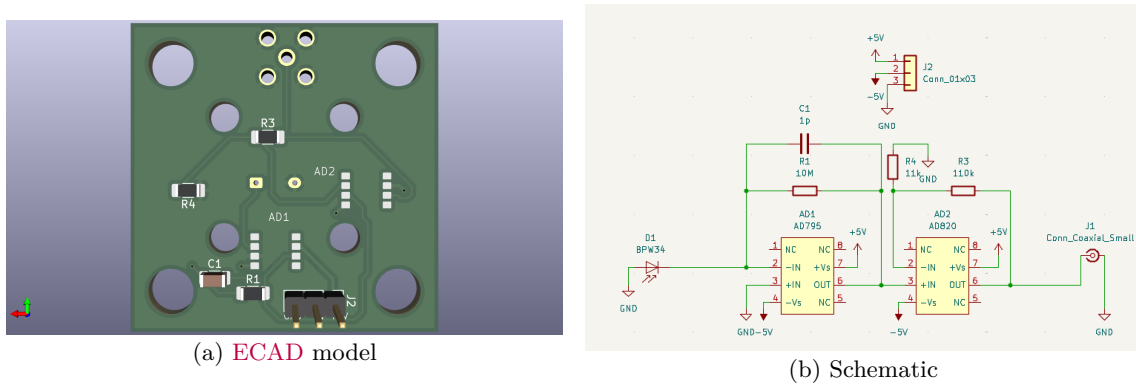


Figure 5.26: Second iteration of the photodetection PCB

Due to the fact that the topology of the first iteration was kept, the **PCB** does not need any modifications in order to work with the circuit parameters. However, after a discussion with the client, a ground plane was added. Usually such an addition would be needed in high-speed and/or high-power use cases, but the circuit only deals with low-speed, very-low-power signals. The reason for the ground plane in the updated design is broader quantum protocol support. While **CW-ODMR** operates at low frequencies, future expansion of the sensing setup might require support for different high-speed pulsing sequences. In that case, the component values can be modified again, without the need for making a new board. Figure 5.26a shows the new board design. The updated board also has better routing than the previous version, which was done to optimize the noise performance.

5.4.3 Third iteration

The third version has an optimized power system that employs a TPS60400 charge pump to invert the 5 V power supplied to it. The charge pump, combined with the fixed board dimensions, made it more difficult to do the placing and routing. Additionally, the clearance of the power and ground nets was increased. Figure 5.27 shows the **ECAD** view of the third iteration of the photodetector.

5.4.4 Fourth iteration

This iteration of the photodetector is less concerned with minor improvements and adaptations for the sensing setup than the previous iterations. In fact, the differences are so significant that the fourth photodetector version requires mostly new components. Instead of an AD795-based **TIA** and an AD820-based post-amplifier, the fourth iteration uses ADA4637 and ADA4627 op-amps. The ADA4637 offers significantly higher **GBP** (79 MHz in comparison to 1,6 MHz), however there is an increase in the noise levels (see Figure 5.29) and this is why it was used for the **TIA**. The

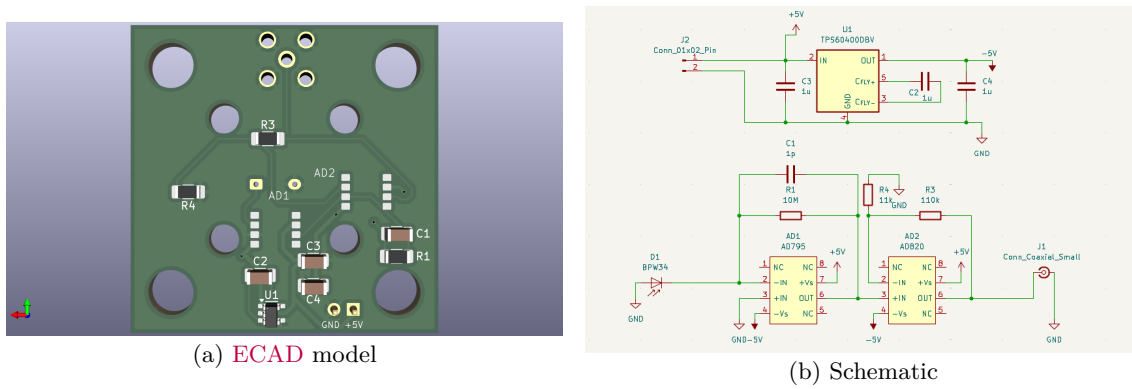


Figure 5.27: Second iteration of the photodetection PCB

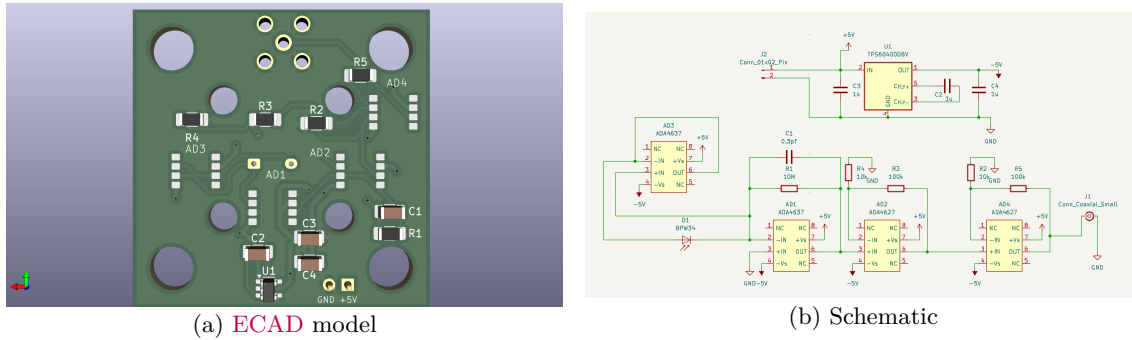
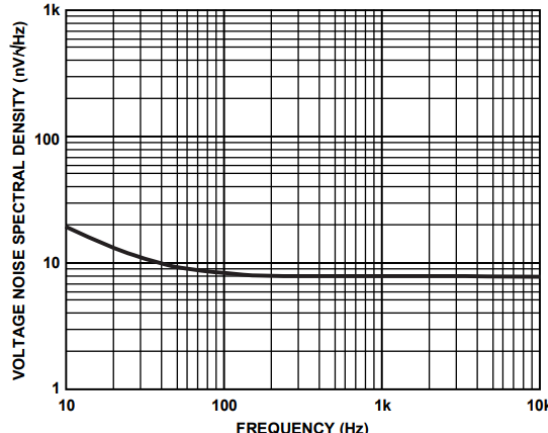
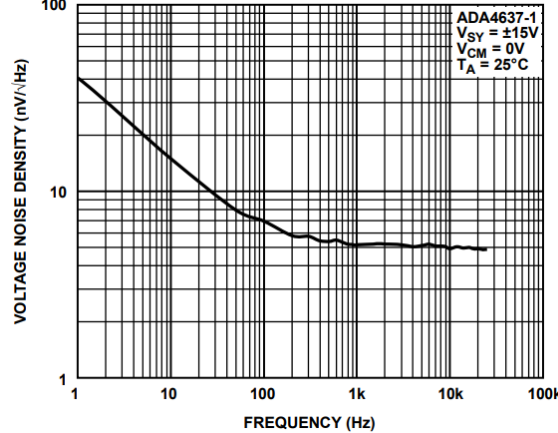


Figure 5.28: Second iteration of the photodetection PCB



(a) Noise spectral density of the AD795 (image credit to the AD795 documentation [18])



(b) Noise spectral density of the ADA4637 (image credit to the ADA4637 documentation [34])

Figure 5.29: Noise spectral density of the amplifiers used in the TIA circuit of the photodetector

bootstrap buffer was also matched to use the same op-amp. An amplifier of the same family, namely the ADA4627, is employed by the output stages, because of its much better noise performance⁹. Decreasing noise later in the signal chain is crucial to maintaining a clear output. With all these considerations in mind, the circuit was designed in a similar manner to the previous iterations (see Figure 5.28).

⁹The ADA4627 has $16 \text{ nV Hz}^{-0.5}$ at 1 Hz, which steadily decreases to $5 \text{ nV Hz}^{-0.5}$ at 10 kHz. The AD820 has $100 \text{ nV Hz}^{-0.5}$ at 1 Hz, which, similar to the ADA4627, decreases to $15 \text{ nV Hz}^{-0.5}$ at 10 kHz. The ADA4637 was also considered as an option for the non-inverting stages, but its noise is higher than the ADA4627

Chapter 6

Testing and results

Table 6.1 shows all the tasks discussed in Chapter 3.4.2 and their current status. While working on the project, the client decided that purchasing a lock-in amplifier is more worthwhile than implementing OLIA, which is why tasks associated with its implementation are marked as canceled. The items with a reassigned status were given over to two students, who are also involved with the quantum sensing setup. The laser driver was reassigned, because a completely new design was needed, the making of which would require too much time. The pulse sequence script was finished and it was passed on to one of the other students for further refinement and possibly for the implementation of different protocols.

Number	Task	Status
1.1	Design photodetector	Completed
1.2	Build OLIA	Canceled
1.3	Set up laser driver	Partially completed; reassigned
2.1	Develop data acquisition software	Canceled
2.2	Program pulse sequences	Mostly completed; reassigned
3.1	Compare lock-in amplifiers	Canceled
3.2	Test quantum sensing setup	In-progress

Table 6.1: List of tasks and their completion status

6.1 Test goals

There are two suitable methods of characterizing the TIA. As the main point of interest is the linearity of the amplifier, the first characterization method is to simulate photodiode readings at different light intensities by modeling it as a current source. By varying the diode model current, either by sweeps or manually, the performance of the physical device can be compared to the simulations.

The second method supplements the results of the first one. It involves measuring the scattering parameters S_{11} and S_{21} and calculating the frequency response of the system. Equation (6.1) shows the formula used to approximate the transimpedance Z_t for a load resistor R_l [23]. This method provides a better overview of the transimpedance over the whole bandwidth of the photodetector.

$$Z_t(f) \approx \frac{S_{21}(f)R_l}{1 - S_{11}(f)} \quad (6.1)$$

Neither of these methods uses a real photodiode, which is why an integration test is also necessary. Not only is the integration test needed to evaluate the performance of the diode, but it also gives insight into how the diode interacts with the laser, which will be used to conduct experiments with the sensing setup. Using the laser driver, a square-wave signal is pulsed at different frequencies within the amplifier bandwidth. By comparing the signal output by the photodetector to the signal output by the function generator, the performance of the system can be determined. Although the laser pulsing limits the test to square waves only, the filtering of high-frequency components at near-cutoff frequencies gives a deeper understanding of the behavior of the circuit.

6.2 Test setup

As different test methods require slightly different physical setups, this section outlines the parts comprising the setups and how they operate. Each setup is dissected separately and the necessary devices and components are shown in diagrams and pictures.

6.2.1 Photodiode-model characterization

Characterizing the system well requires fixed currents, due to the big difference in output voltage small currents differences at the input make. As the diode detects ambient light and cannot be set to one current level reliably, a model needs to be used instead. A voltage source can then be used to simulate the nanoampere photovoltaic current I_f generated by the diode. According to Säckinger [23], the resistor R_d and the capacitor C_d in Figure 6.1 are enough to characterize a TIA circuit. By inputting a voltage at the node V_i , R_d functions as a current source, similar to a photodiode. This model assumes the parallel shunt resistance is so high that it can be omitted, while the series resistance can be neglected due to its limited impact on the system. However the diode capacitance is central to TIA analysis and design, which is why C_d is there to mimic it. Additionally, the matching resistor R_i can be replaced by a coaxial terminator and the capacitor C_i is used to isolate the input from the rest of the circuit.

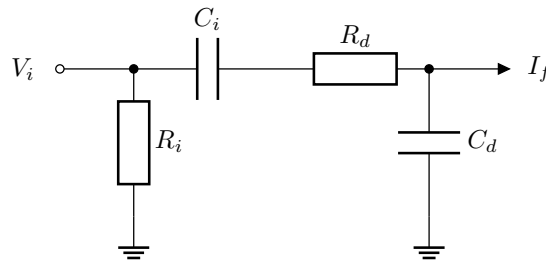


Figure 6.1: Photodiode model

Using this model, the diode current I_f can be approximated using Equation (6.2). The approximation is true only if the input impedance Z_i (see Equation (6.3)) of the TIA is significantly lower than R_d [35]. Keeping this in mind, a resistor six to seven orders of magnitude bigger was selected for the physical circuit.

$$I_f = \frac{V_i}{R_d} \quad (6.2)$$

$$Z_i = \frac{R_1}{A_o + 1} \quad (6.3)$$

Finally, the full setup diagram can be seen in Figure 6.2. Using the function generator feature of the Analog Discovery 2, a voltage can be generated and, using the current through R_d , the oscilloscope output can be used to characterize the system.

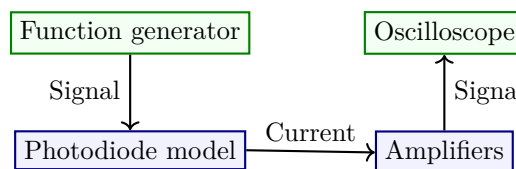


Figure 6.2: TIA characterization with photodiode model test setup diagram

For the tests, it was decided to test the DC characteristics of the amplifier separately from the frequency response. Because of C_i , a DC voltage will not generate a current. Instead, to verify that the DC amplification matches the simulations, a low-frequency sine wave is used and its amplitude is varied, all while the output voltage is measured. The frequency response test measures the response of the system at near-cutoff frequencies, similar to the integration test. The difference is that instead of pulsing the laser, sine waves generate current using the photodiode model, which is then amplified. The change of waveforms is necessary because of the distorting effect of C_i on square waves, especially at lower frequencies.

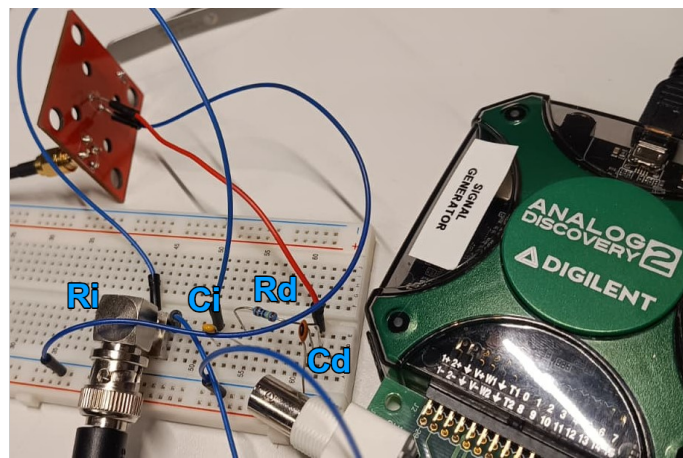


Figure 6.3: Photodiode model test setup

Figure 6.3 shows the assembled setup. A $1\text{ M}\Omega$ resistor was used for R_d . Although the diode capacitance C_d is very important for the frequency response, a 27 pF capacitor was used instead of a 25 pF one. This small of a difference should not affect the results much.

6.2.2 S-parameter characterization

Scattering parameters, also known S-parameters, are often used to characterize Radio-Frequency (RF) circuits and antennas by using a Vector Network Analyzer (VNA). For this particular test, the S_{11} and S_{21} parameters are needed to calculate the transimpedance using Equation (6.1). In order to measure both, the VNA needs to be configured as shown in Figure 6.4. S_{11} can be measured with only port 1 of the VNA being connected to the photodetector. However, port 2 is needed to measure S_{21} at the output of the photodetector.

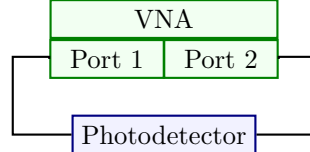


Figure 6.4: S-parameter characterization of a TIA using a two-port VNA

6.2.3 Integration test

The integration test has a similar test setup to the complete quantum sensing setup. However, the light from the laser directly illuminates the photodiode instead of a diamond sample NV. This was done on purpose, because this test layout provides realistic information on the functioning of the photodetector when used in the quantum sensing setup. This test is particularly interesting for pulsed protocols, as a photodetector for them needs to be able to have a well-defined rising edge. A filter was placed in front of the photodiode to remove the green component of the laser and reduce the overall light intensity. However, some of the tests were done without filtering, as with manual adjustment the light intensity at the sensor can be set to an ideal level. When the tests were done, the new version of the laser driver was available and its PCB included a laser, as seen in Figure 6.5.

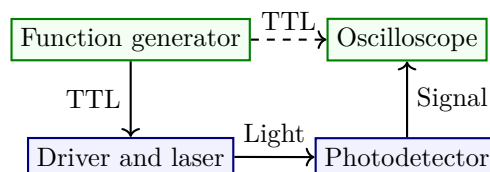


Figure 6.5: Integration test setup diagram

In addition to the diagram, Figure 6.6 shows what the physical measurement setup looks like. Because of reasons discussed in the section containing the results (see Chapter 6.3.3), the distance between the laser and the detector had to be increased and the alignment manually adjusted.

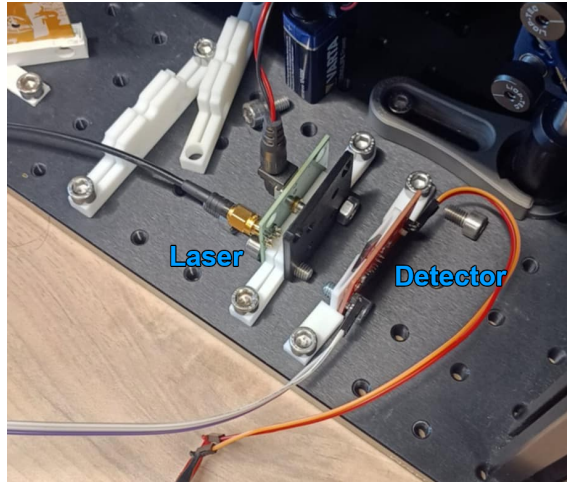


Figure 6.6: Integration test setup

6.3 Results

This section of the report covers the previously discussed tests and provides images of the measurements. Furthermore, the simulation results are also used for comparison.

6.3.1 Photodiode-model characterization

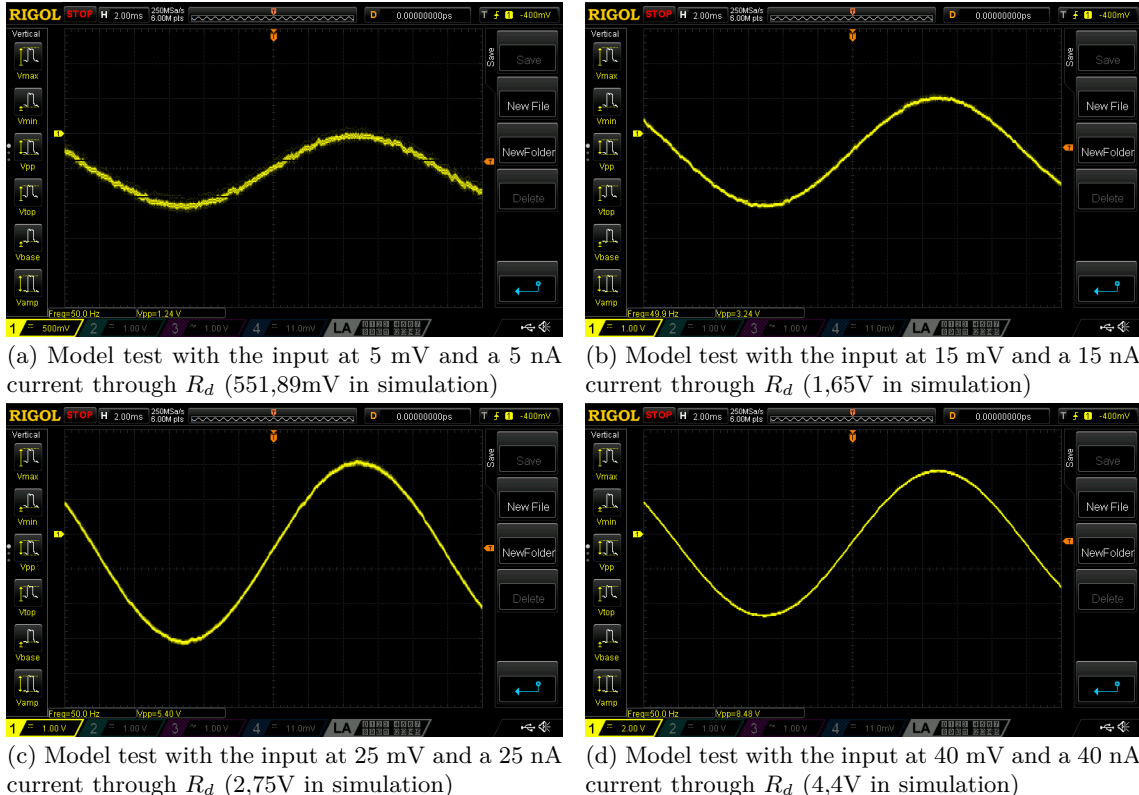


Figure 6.7: DC characteristics test with a photodiode model ($R_d = 1 \text{ M}\Omega$, $C_d = 27 \text{ pF}$) of the first iteration of the photodetector with a 50 Hz input signal

Figure 6.7 shows how the first iteration of the photodetector performed under the photodiode model test. In the plots, the amplitude, or half of the peak-to-peak voltage, corresponds to the output signal magnitude that needs to be compared to the simulations. Knowing this, it is clear that the system displays the expected linear behavior¹.

To gain a better understanding of the noise, it was measured with the diode model connected, but turned off. The results are shown in Figure 6.8 and show sporadic changes in voltage with no discernible periodic component, which means the noise is most likely caused by the diode model and significantly amplified by the amplifiers.



Figure 6.8: Noise of the first iteration when connected to the diode model

Figure 6.9 shows that the first version of the photodetector exhibits slightly more attenuation at near-cutoff frequencies than expected. Simulations were conducted and they verified that the main cause was not the slightly larger C_d . Its increase only accounts for around 100 Hz of difference in the bandwidth. It is possible that parasitic capacitance, which were not accounted for, are present, which would explain the slight bandwidth reduction.

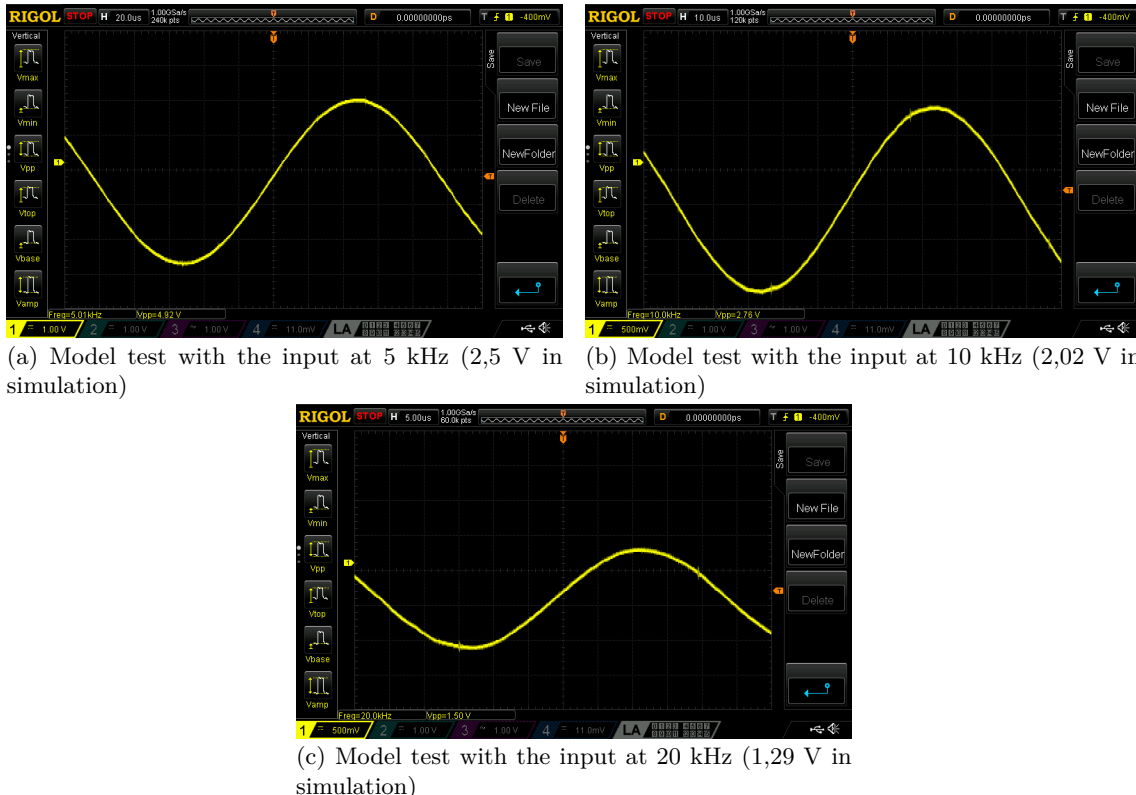


Figure 6.9: Near-cutoff characteristics test with a photodiode model ($R_d = 1 \text{ M}\Omega$, $C_d = 27 \text{ pF}$) of the first iteration of the photodetector with a 25 nA input signal

Figure 6.10 shows the results of the DC characteristics tests of the second version of the photodiode. Despite the measurements showing results similar to the simulations, the output signal

¹It should be noted that the V_{pp} values shown in the oscilloscope measurements are approximate. During the tests, it was determined that they can deviate as much as 15% from the signal value

contains significant amounts of noise, which exceed the expected levels. Furthermore, the noise of the system is more pronounced than the first iteration, which was also unexpected.

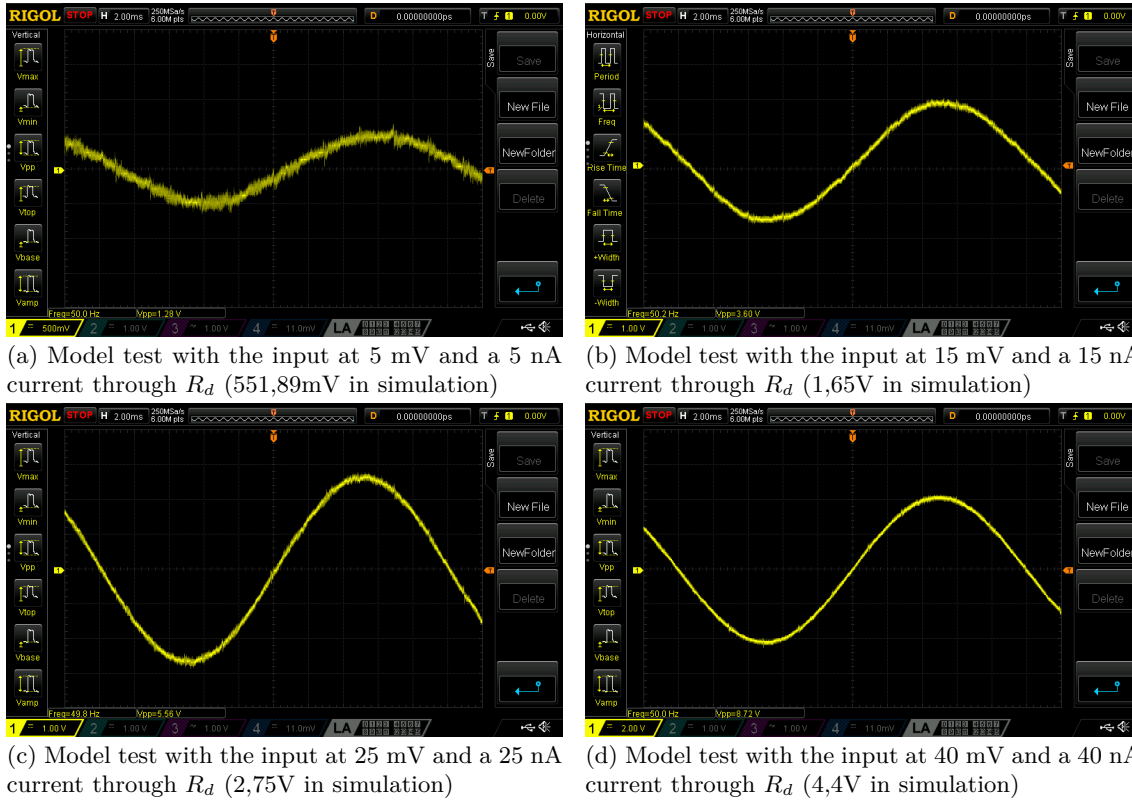


Figure 6.10: DC characteristics test with a photodiode model ($R_d = 1 \text{ M}\Omega$, $C_d = 27 \text{ pF}$) of the second iteration of the photodetector with a 50 Hz input signal

The noise, seen in Figure 6.11, is not dominated by a periodic signal, which means it is generated by environmental sources. Interestingly, the noise floor of the second iteration is higher than the first one. With the improved layout and added ground plane, the second iteration was expected to have better noise characteristics. It is possible that the increased bandwidth contributes to the noise, but its effect should be minimal. While testing, it was also determined that there were issues with the power connection, which contributed significant noise to the signal, as well.



Figure 6.11: Noise of the second iteration when connected to the diode model

Similar to the first version, this one exhibits more attenuation at near-cutoff frequencies. That being said, there increase in bandwidth can be seen clearly, in spite of the the excessive attenuation.

The tests of the third iteration of the photodetector, seen in Figure 6.13, show that the amplifier has a similar performance to the previous iteration. It does have more noise, but with the addition of the charge pump, the increase in noise was expected. Otherwise, both the second and the third version demonstrate the same amplification at all current levels.

What is more interesting about the tests of the third version of the photodetector is the noise. Figure 6.14 shows that compared to the previous version, which lacks a charge pump, this iteration has a barely-noticeable periodic signal present even when there is no input voltage from the Analog

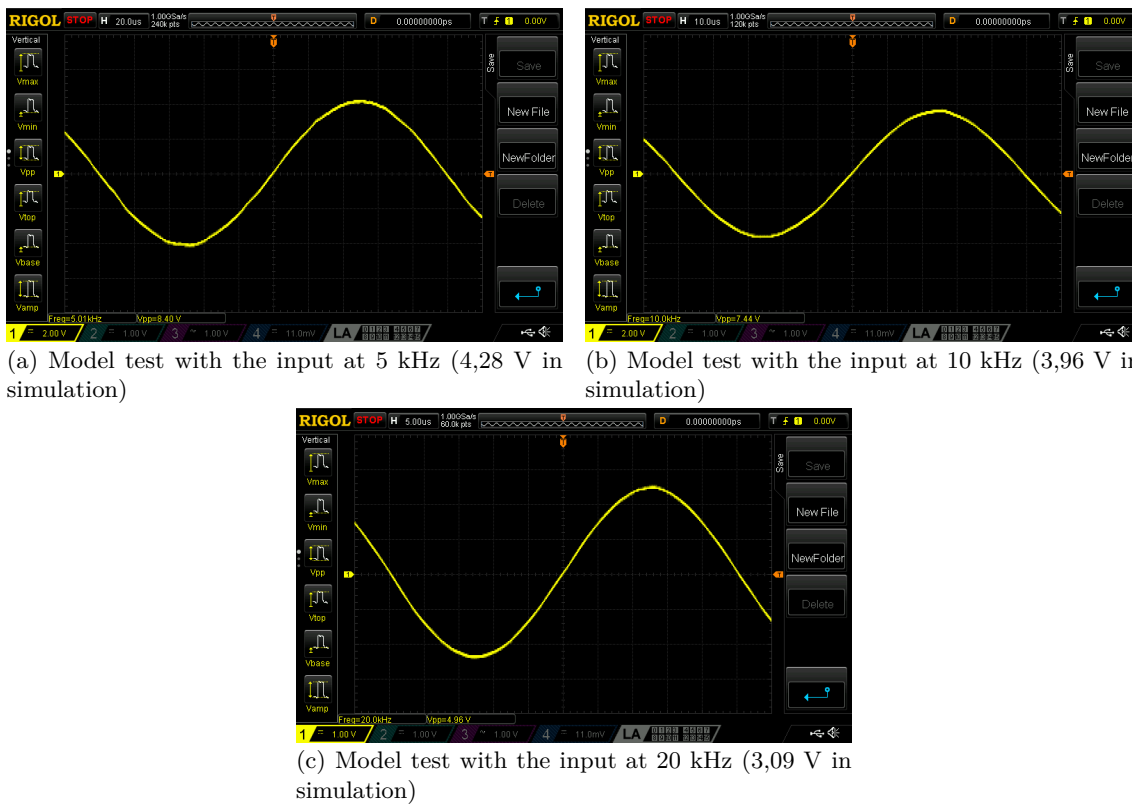


Figure 6.12: Near-cutoff characteristics test with a photodiode model ($R_d = 1 \text{ M}\Omega$, $C_d = 27 \text{ pF}$) of the second iteration of the photodetector with a 40 nA input signal

Discovery. Because the integration tests in Chapter 6.3.3 demonstrate the noise more clearly, detailed examination of charge pump noise is left for later.

As expected the near-cutoff behavior of the third version of the system is almost identical to the second one, as seen in Figure 6.15. What is more interesting about the plots is that there is a clear periodic signal in addition to the noise, especially in Figures 6.15a and 6.15b.

6.3.2 S-parameter characterization

Unfortunately, the system could not be characterized by means of S-parameters. This is due to the lack of suitable equipment. The laboratory had a VNA that could only be used to measure S-parameters in the RF range. There was another method which was tried, which involves using the waveform and oscilloscope channels of an Analog Discovery 2 as a VNA. While this method can cover the operating frequencies of the device, it can only measure the S_{11} parameter of the device, because it functions as a network analyzer with a single port. Lastly, attempts at contacting researchers from the University of Twente for their equipment were made, but they did not respond.

6.3.3 Integration test

Tests were originally done with the laser placed less than 1 cm away from the photodiode. However, better measurements can be achieved by moving the laser further away and not aligning the center of the beam with the diode. Doing both reduces the light intensity at the photodiode, which in turn prevents the sensor from being overexposed. In photovoltaic mode, overexposure severely lengthens the rise and fall time of the photodiode, and this effect is further exacerbated by the extremely high sensitivity of the circuit. Figure 6.16 shows how the photodetector performs under close to ideal conditions. In these tests, the laser intensity should be barely enough for the signal to exhibit supply clipping.

The measurements of the first iteration of the photodetector present a cleaner response at higher frequency, but the low-frequency measurement in Figure 6.16a demonstrates the effect of ambient light, as well as electrical interference, on the circuit. When there is no direct laser light present, the photocurrent still generated over 200 mV of voltage. This effect is not noticeable in the higher-frequency measurements, however, they demonstrate a significant increase in signal rise

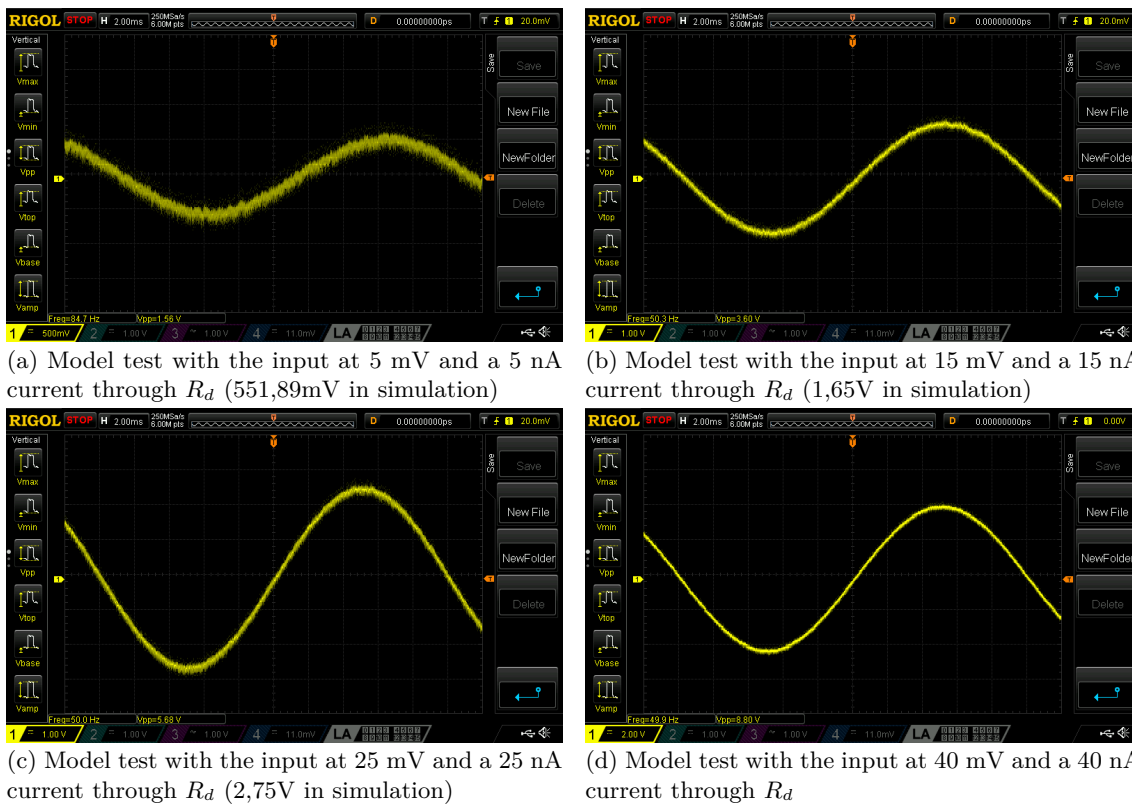


Figure 6.13: DC characteristics test with a photodiode model ($R_d = 1 \text{ M}\Omega$, $C_d = 27 \text{ pF}$) of the third iteration of the photodetector with a 50 Hz input signal



Figure 6.14: Noise of the second iteration when connected to the diode model

and fall time.

The same test was ran on the second version of the photodetector and the results are shown in Figure 6.17. In comparison to the first iteration, there is noticeable reduction in low-frequency noise at 50 Hz (Figure 6.17a). Furthermore, the high-frequency performance has also improved in the second version. The 5 kHz measurements in Figure 6.17b show significantly better waveform definition. What is more, at 10 kHz there is less high-frequency noise, in comparison to before, as can be seen in Figure 6.17c. Similarly, the 20 kHz signal in Figure 6.17d demonstrates a decrease in noise, but it also shows off the increase in bandwidth. Whereas the first iteration amplifies the signal to 2,1 V peak-to-peak, the second iteration outputs a 4 V signal.

In Figure 6.18, the third version of the photodetector demonstrates better high-frequency performance and slightly better low-frequency noise attenuation than the first version, but it still performs worse than the second one. Figure 6.18a shows marginally less noise at 50 Hz, in comparison with the first iteration, but there is significantly more high-frequency noise than the second iteration. This can be seen when the laser is off. Figures 6.18b and 6.18c show well-defined pulse edges at 5 kHz and 10 kHz respectively, but, when compared to the 4,8 V signal of the second iteration, it is clear that the peak-to-peak voltage of 3,7 V is much smaller than it should be. Lastly, the signal in Figure 6.18d demonstrates similar edge definition to the second iteration. However, the magnitude of the signal is significantly lower at 2,6 V peak-to-peak, in comparison to 4 V.

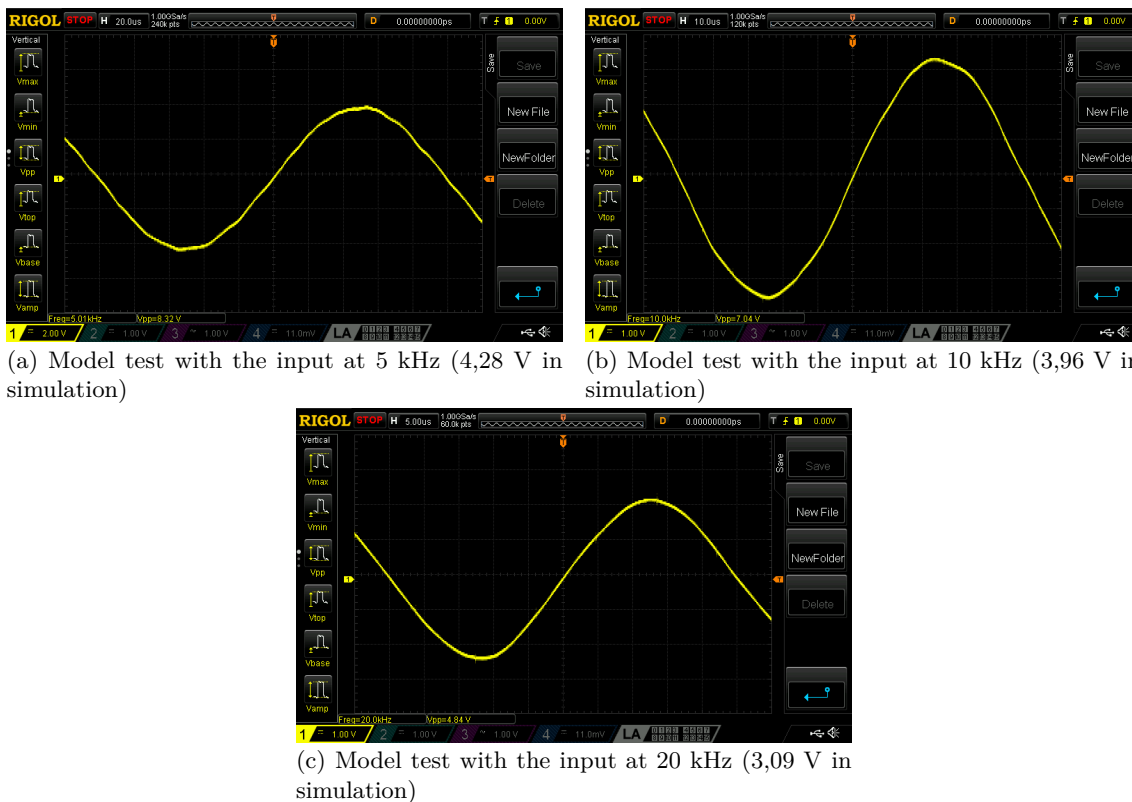


Figure 6.15: Near-cutoff characteristics test with a photodiode model ($R_d = 1 \text{ M}\Omega$, $C_d = 27 \text{ pF}$) of the third iteration of the photodetector with a 40 nA input signal

Lastly, at all test frequencies, there is a significant amount of noise present and its shape, as well as its frequency, suggest the noise originates from the charge pump.

Figure 6.19a shows the supply noise seen at the output, which reaches up to 400 mV and has a frequency of 50 kHz. Because the signal containing the noise suggests insufficient supply filtering, the capacitances C_O , C_{fly} and C_I (see Figure 5.10) were increased to 10 pF, which is 10 times bigger than what the manufacturer recommends and what was used previously. This resulted in a significant improvement, as can be seen in Figure 6.19b, with the new peak-to-peak maximum being 80 mV.

After changing the filtering capacitors, the laser pulsing tests were done again and the results are shown in Figure 6.20.

The results in Figure 6.20 show the expected noise improvement. At 50 Hz (see Figure 6.20a), the low-frequency noise is much more evident than supply noise in the signal when the laser is off. However, the high-frequency noise is still apparent at 5 kHz. Curiously, at 10 kHz, the peak-to-peak voltage increased from 3,3 to 4,5 V. Similarly, at 20 kHz increased from 2,7 to 3,8 V, which is still slightly less than the output of the second iteration (4 V).

Lastly, Figure 6.21 shows the results of the integration test of the fourth version of the photodetector. They clearly demonstrate a much lower gain than expected, even when the diode is illuminated directly. Additionally, the output signals are much more distorted than the previous versions and the cutoff frequency is much lower than expected. That being said, the noise levels are still within the expected range.

The most likely explanation for the bad results is the photodiode biasing. While in theory there is not voltage drop over a photodiode when in photovoltaic mode, in practice there are several millivolts of voltage across the diode, which still set the bias of the photodiode. According to Säckinger [23], this voltage greatly diminishes when a bootstrap is implemented and as a result the output current diminishes. This would explain the decrease in amplitude and the distorted shapes of the waveforms. To remedy this, a. shown in Figure ??

6.3.4 Additional integration test

During the integration test it was observed that the green laser has such high intensity, that it easily lead to overexposure. Experiments continued to show high intensity, even after putting an optical

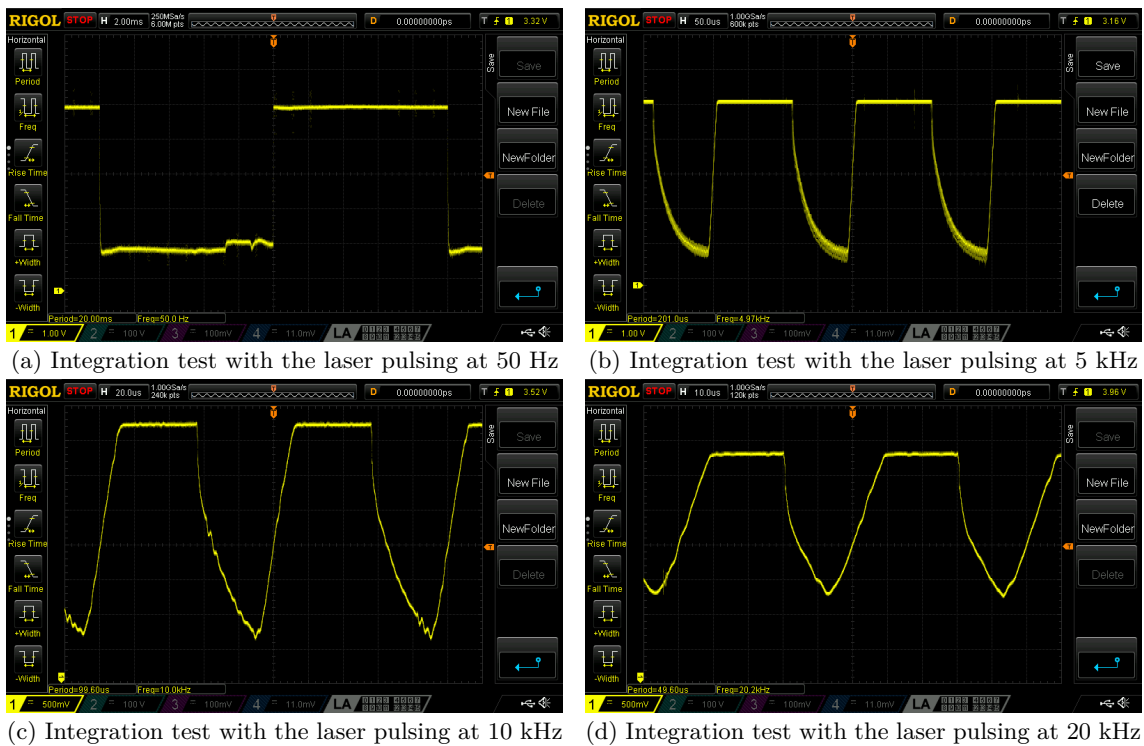


Figure 6.16: Integration test of the first iteration of the photodetector (cutoff frequency $f_c = 10,77$ kHz) with an unfocused medium-distance laser

filter before the detector. Ideally, no light from the laser should be present at the output when conducting quantum protocols, but real-world setups have small amounts of laser light present in the output signal. Because of this, it was decided that measurements of the laser levels with optical filters were needed for future reference when integrating the setup.

To simulate a compact integration of the setup, the laser was placed as shown in Figure 6.23. However, as discussed previously, close proximity from the laser and direct illumination of the sensor result in overexposure. In a functional setup, the laser light will be filtered, as a result of which the intensity of the green light will be decreased.

Figure 6.24 shows the specifications of the laser used in the integration tests, as well as the optical filter. Because the laser emits light with an intensity of approximately 520 nm, the filter should block the light from it almost completely. To best test the filters, it was decided that the most suitable frequency for the tests is 5 kHz. It is high enough for the unfiltered sensor to be so overexposed that it only outputs a DC voltage, but it is not high enough for near-cutoff behavior to affect the results.

Contrary to what was expected, the tests, shown in Figure 6.25 demonstrate poor filtering. When testing with a single filter, there is not only clipping, but also overexposure of the sensor. This is apparent from the signal in Figure 6.25a, as it resembles a Pulse-Width Modulated (PWM) signal with a duty cycle of over 60 %. As a result, there is also a large overshoot after the falling edge. The results of the test with two stacked filters are better, but not enough for quantum sensing protocols. As can be seen in Figure 6.25b, the signal still clips. This makes it impossible to execute any quantum protocol, as no fluorescence can be measured when the amplifier output has hit the maximum. Even worse than the clipping is the fact the photodiode is still slightly overexposed. Despite the reasonable shape of the signal, the width of the pulses is still slightly wider than the ideal. Furthermore, there is a slight overshoot, which can be seen after the falling edge. Ultimately, both setups show suboptimal filtering, which causes signal clipping and overexposure of the sensor.

6.4 Discussion

As a result of the tests, it was concluded that even the first iteration of the photodetector can be used for CW-ODMR measurements. The protocol can be executed with extremely-low-bandwidth photodetectors (e.g. 18 Hz [16]). That being said, pulsed protocols cannot be achieved with the first iteration of the circuit due to their high frequency requirements. Higher frequencies also exacerbate

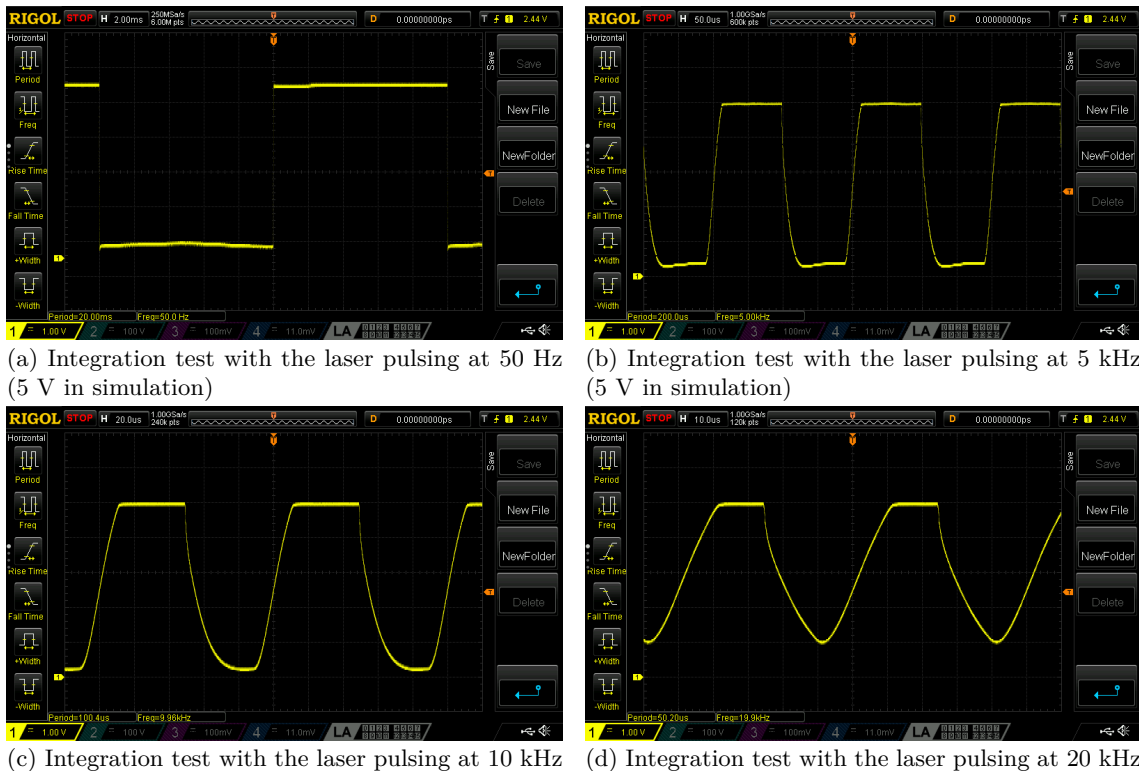


Figure 6.17: Integration test of the second iteration of the photodetector (cutoff frequency $f_c = 21,167$ kHz) with an unfocused medium-distance laser

the issue of overexposure of the sensor, which leads to decreased performance. The effect of the laser on the sensor needs to be considered when integrating the complete setup, as it can affect the measurements. There are cancellation techniques to measure only the NV luminescence [4], but if the photodiode is overexposed or the signal is getting limited by the power rail, the output will not be usable.

Even though the first iteration has passable characteristics, it is worse than the second version in all regards. The improved TIA design presents a better frequency response. Across all frequencies, the device shows less attenuation of the harmonics of the square wave, as well as more defined rising and falling edges. In addition, there is less noise present in the signal. This can be attributed to the addition of the ground plane, as well as the better layout of the PCB.

The third iteration offers a solution that is more suitable for a compact setup. The frequency response is the same as the second version, but the onboard power supply inverter generates unwanted noise. As seen in Figure 6.19, there is a large periodic signal, that looks like a supply ripple. It is also possible that the 1 μ F filtering capacitors C_O , C_I and C_{fly} do not match the design values, because they were found in a capacitor book in the FabLab. Due to the unknown manufacturer and model, the ESR of C_O might also be too big. Furthermore, there is a possibility that their capacitance is lower than 1 μ F, which would also explain the shape of the ripple in Figure 6.19a. The presence of 50 kHz noise after increasing the capacitance, in combination with the large noise amplitude, suggests there is interference with the output of the amplifier.

6.5 Known limitations

The most obvious limitation is the lack of equipment for some tests, which lead to using less appropriate alternatives or having to cancel tests. For example, due to the lack of a suitable VNA, the only method for circuit characterization was using a diode model. The latter would also benefit from a real nanoampere current source instead of the makeshift source that had to be used. The diode model using the 1 $M\Omega$ resistor also contributed significantly, which was amplified by the TIA.

There are many factors that affect the measurements, but perhaps most prominent are the environmental lighting sources, at least when it comes to the integration tests. This includes ambient sunlight, which gets through the blinds of the lab, and reflections from the laser. Both significantly affect the photodetector, especially when there is no focused light present. Reflections,

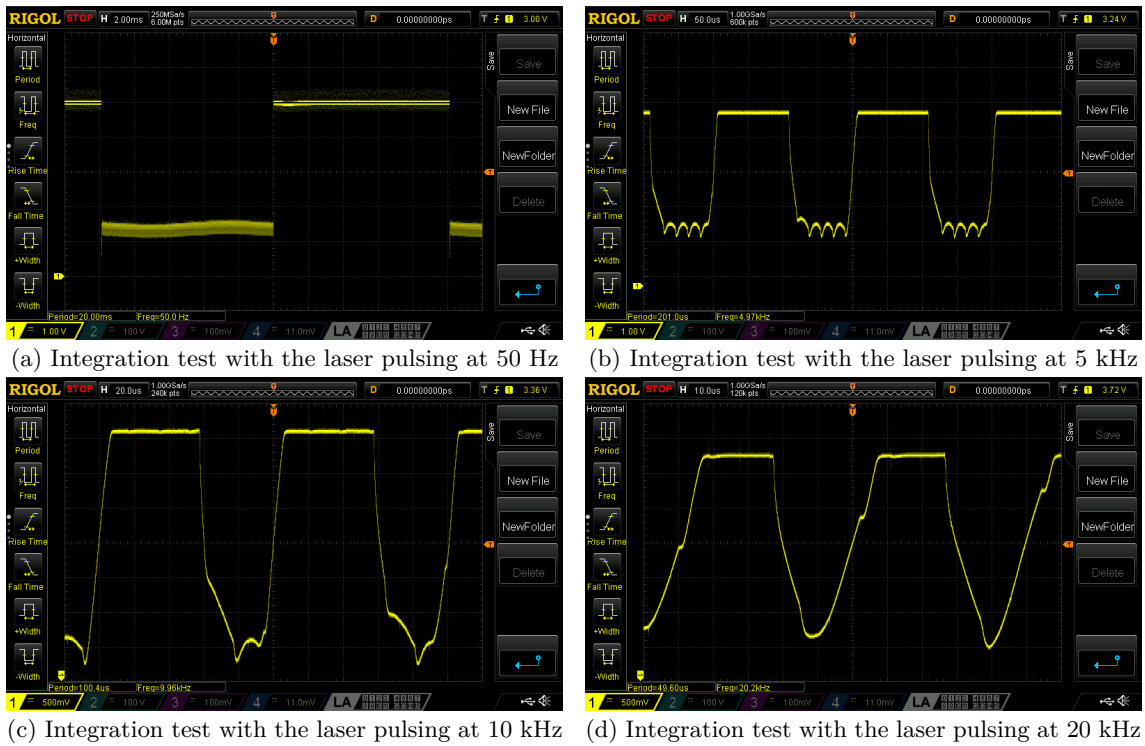


Figure 6.18: Integration test of the third iteration of the photodetector (cutoff frequency $f_c = 21,167$ kHz) with an unfocused medium-distance laser

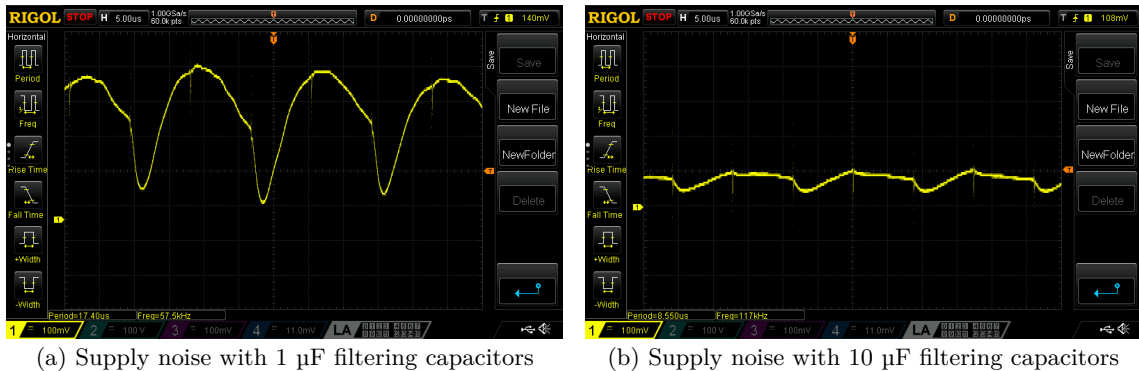


Figure 6.19: Noise measurements in minimal-lighting conditions of the third iteration of the photodetector

in particular, majorly contributed to signal distortion at higher frequencies.

Furthermore, the light source in the medium-distance integration tests had to be manually adjusted, meaning that the output signals do not represent the ideal performance. In fact, the measurements present results with slight power rail clipping, which is unavoidable with the testing setup. To achieve ideal readings, the laser would have to be affixed and the orientation adjusted, while the intensity at the given distance is measured.

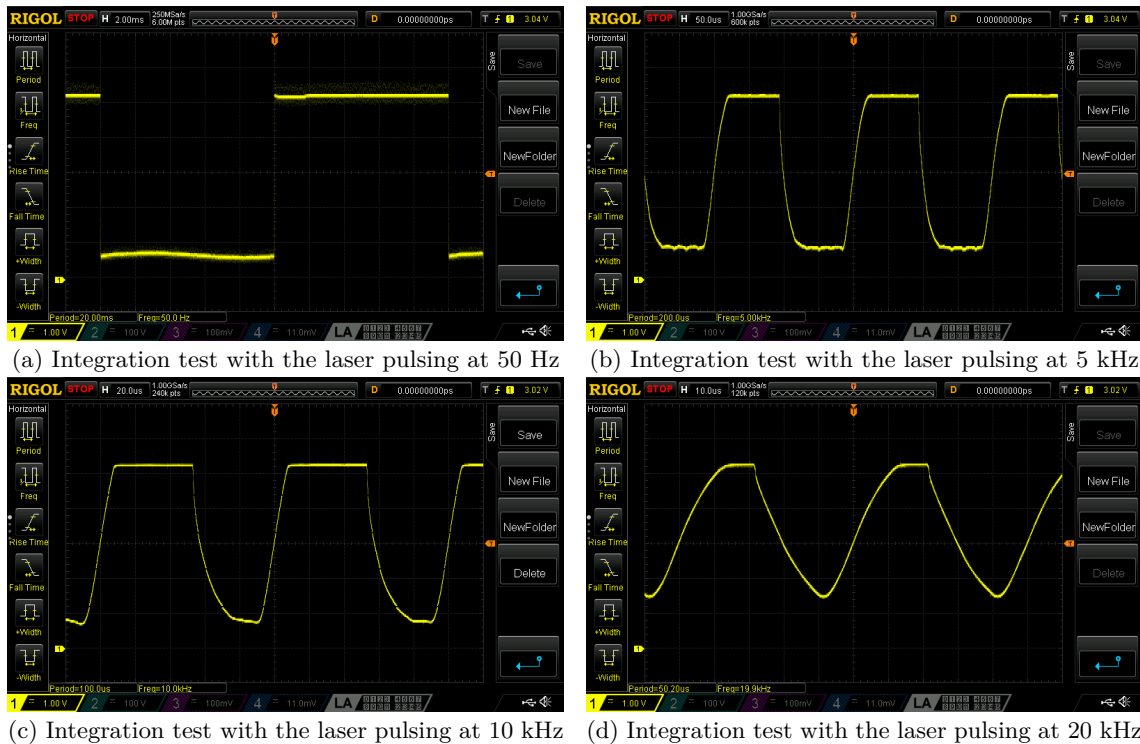


Figure 6.20: Integration test of the modified (increased power filtering capacitors) third iteration of the photodetector (cutoff frequency $f_c = 21,167$ kHz) with an unfocused medium-distance laser

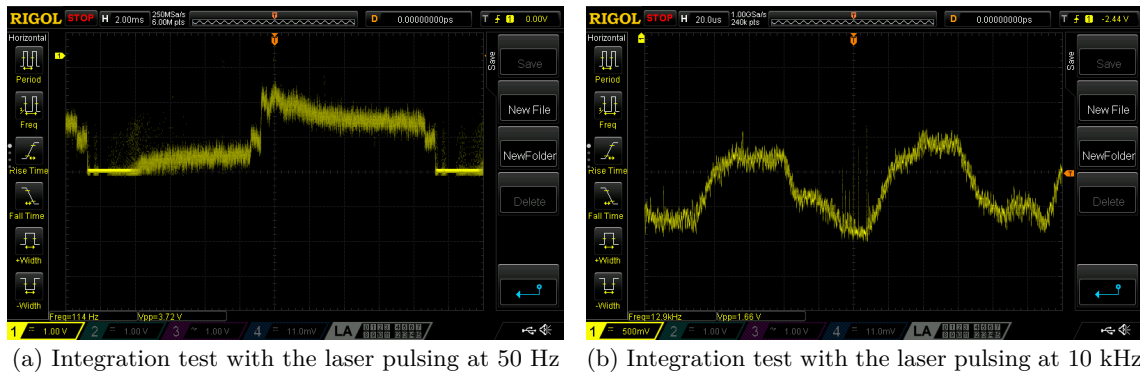


Figure 6.21: Integration test of the fourth iteration of the photodetector (cutoff frequency $f_c = 724,69$ kHz) with an unfocused medium-distance laser

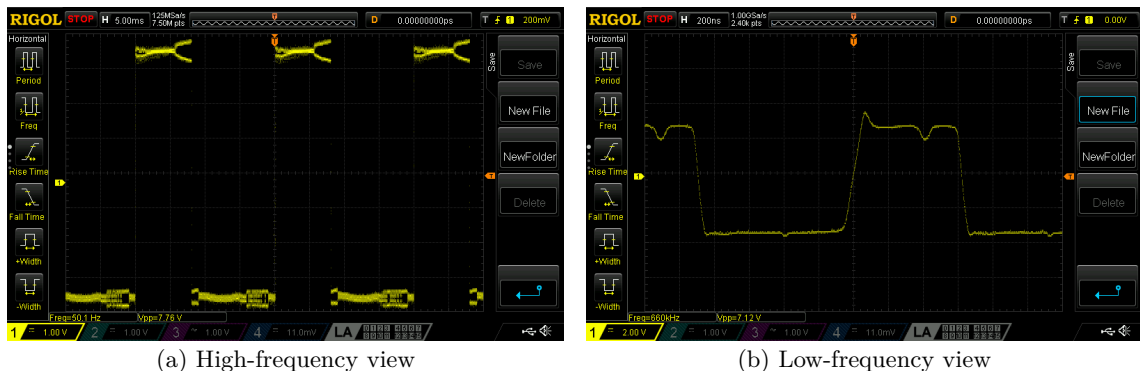


Figure 6.22: Output signal demonstrating photodiode biasing issues when the fourth iteration of the photodetector uses a biasing circuit

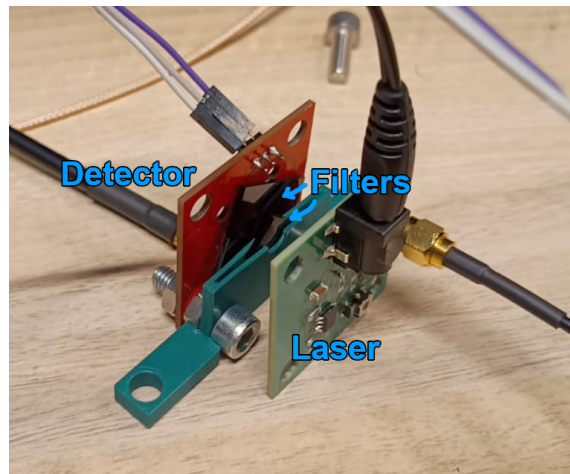


Figure 6.23: Additional integration test setup

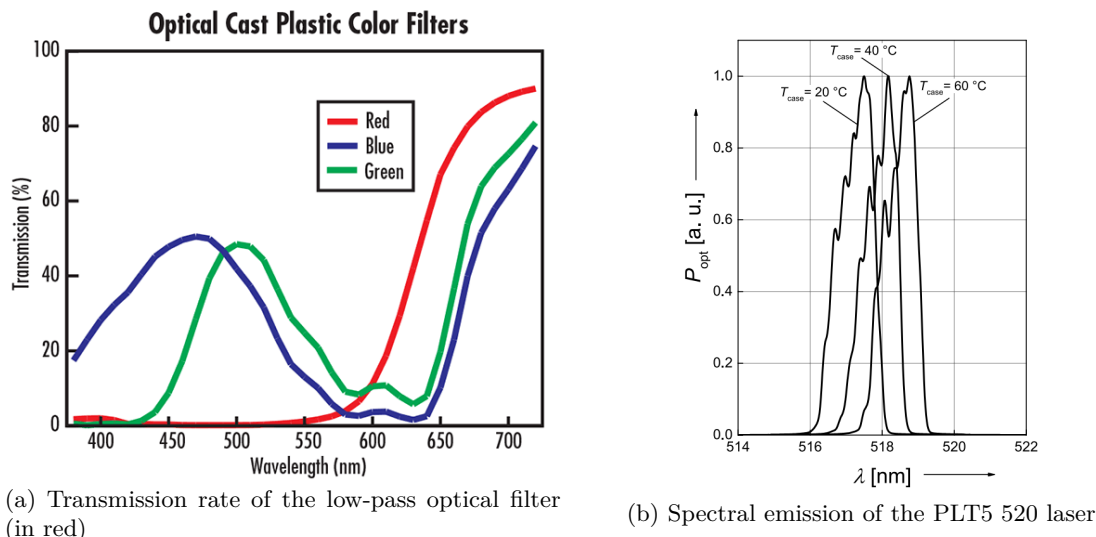


Figure 6.24: Spectral characteristics of the components in the setup

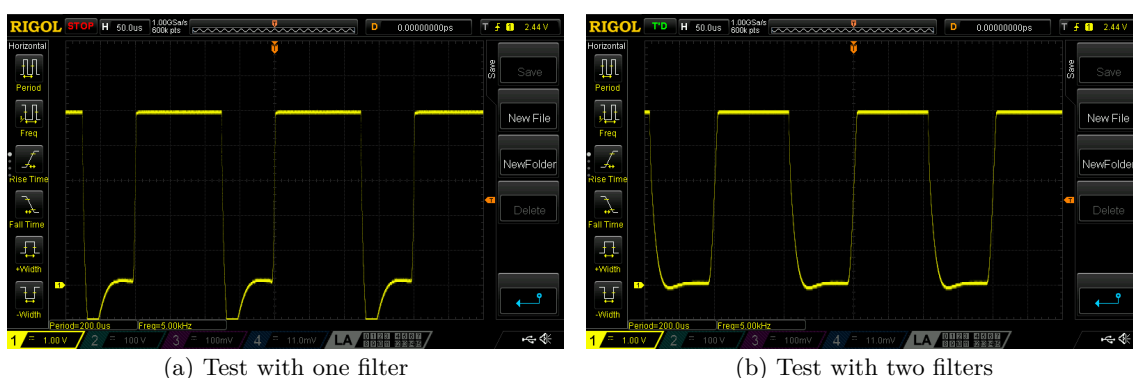


Figure 6.25: Laser transmission tests with the second iteration of the photodetector and laser pulsed at 5 kHz

Chapter 7

Conclusion

In conclusion, the goal of the project, to enable detection of light signals for quantum sensing, was achieved. While there is still work to be done in order to achieve pulsed quantum protocols, the photodetector platform can be used as a reference for future designs.

According to the introduction in Chapter 3, the main purpose of the project was create a photodetector, but integration of the sensing setup was also important. Both were tackled during this project, with the focus being on photodetection. While setup integration also holds importance for the research group, most of the tasks related to it were redistributed among other students. Further refinements to the photodetector and the setup as a whole are possible. Some of the most promising ones are discussed in the recommendations in Chapter 8. Complete integration of the whole setup necessitates more work, but is achievable in the near future.

The first iteration of the photodetector is suitable for **CW-ODMR** measurements with the quantum sensing setup. Despite its functionality, it also presents some minor integration problems, such the need for a dual-rail power supply.

Perhaps most suitable of all for low-noise **CW-ODMR** measurements, the second version showed promising results and is most suited for a lab setup. Out of all improvements, the noise reduction is the most significant. However, the need for a dual-rail power supply limits the usability in more compact and self-contained future implementations.

Version three of the device addresses the major integration concern of having a simple and small power supply solution. At the same time, it also incorporates the improved system response of the second iteration. Although the **Alternating Current (AC)** characteristics of the circuit are irrelevant for **CW-ODMR**, they become the most important aspect of the circuit when discussing pulsed protocols. However, the third version of the photodetector suffers a significant noise problem, caused by the inverting charge pump. Although this is a significant problem, increasing the filtering capacitors showed a major improvement. Even if this version is not recommended for a desktop setup, microcontroller-based portable solutions will benefit from the simplified power supply and will not need an external module to supply -5 V to the detector.

The fourth photodetector iteration presents a solution specifically designed to handle pulsed protocols. Even though the exact frequency and gain requirements for the circuit are unknown¹, the fourth version should be able to do T_1 measurements. Whether higher-frequency pulsed protocols can be achieved is still unknown, as the setup has not been completely integrated.

¹Different papers often present different pulsing specifications. In addition, the client wants to adjust the pulsing specifications, so the necessary photodetector bandwidth can only be estimated

Chapter 8

Recommendations

There are several recommendations that are important for future implementations, as they may contribute to the precision, noise-suppression and stability of the photodetector and the quantum sensing setup as a whole.

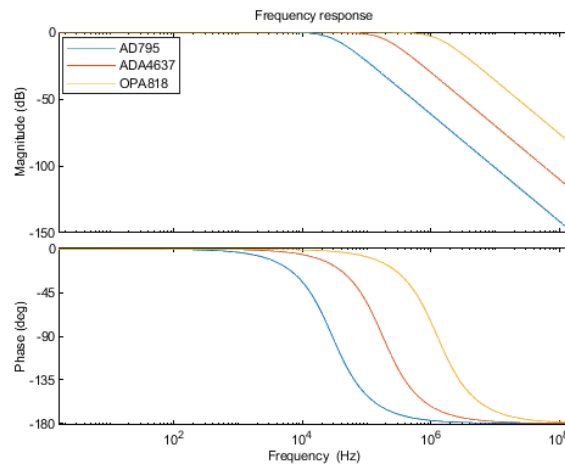
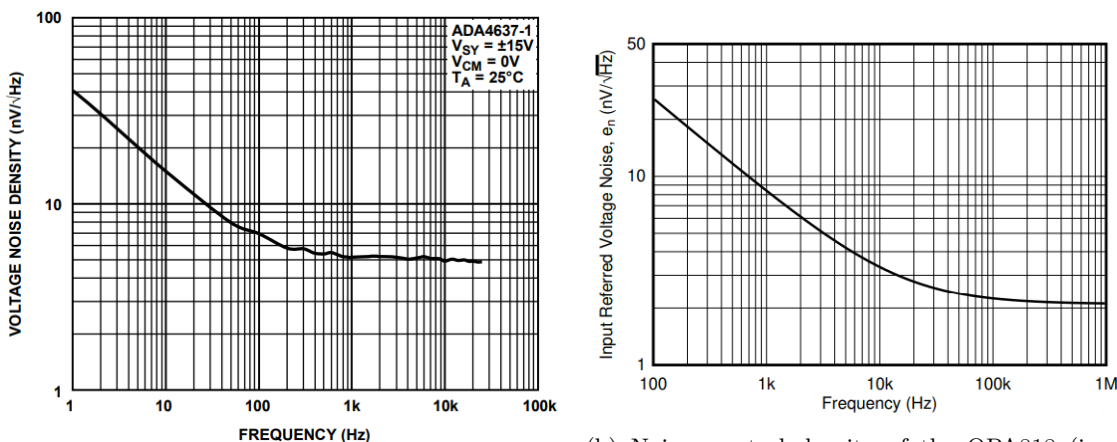


Figure 8.1: Comparison of the Ad795, ADA4637 and OPA818 when configured for 140 dB of transimpedance gain ($R_1 = 10 \text{ M}\Omega$) and a Bessel frequency response

Firstly, increasing the photodetector bandwidth should be the primary concern of the people working on the setup, as no version of the detector can measure Rabi oscillations, which occur at over 3 MHz. Version four of the photodetector has a much wider bandwidth, but it is bottlenecked by the photodiode, which is only stable at up to 350 kHz in the photovoltaic configuration [13]. However, biasing a BPW34 diode in photoconductive mode will result in an increase in dark current, usually around 2 nA, but it can rise up to 30 nA, rendering the actual signal unreadable. Alternatively, the bandwidth can be increased by finding an op-amp with bigger **GBP**. Out of all op-amps that were explored, the OPA818 shows the most promise, which is why its mathematical model was used to compare it to the AD795 and ADA4637. Figure 8.1 showcases the significant bandwidth increase from the ADA4637 to the OPA818. Using the former results in a 138,87 kHz bandwidth, while the latter results in a 982,44 kHz bandwidth. As is usually the case with bigger-**GBP** op-amps, the OPA818 has worse noise parameters ($25 \text{ nV Hz}^{-0.5}$ at 100 Hz as compared to $7 \text{ nV Hz}^{-0.5}$ at 100 Hz).

In the future, if even greater bandwidth is desired, transistor **TIAs** should be investigated. Transistors offer finer control over the parameters of the amplifier they constitute. This is, in part, due to the control over the technology of each transistor, but also because they are lower-level components than op-amps, which allows for more intricate layouts. Several sources on the matter were consulted [23, 37–39], but because of time constraints and equipment availability, an op-amp-based solution was chosen instead.

Secondly, exploring avalanche photodiodes as an alternative to the Si diode (BPW34) currently in use, might contribute to better measurements. Although they are widely used in low-intensity applications, avalanche diodes are quite expensive. The client wanted to keep the cost low for



(a) Noise spectral density of the ADA4637 (image credit to the ADA4637 documentation [34])

(b) Noise spectral density of the OPA818 (image credit to the OPA818 documentation [36])

Figure 8.2: Noise spectral density of the amplifiers used in the **TIA** circuit of the photodetector

this project, but in the future more precise pulsed protocol measurements might benefit from the internal amplification and increased precision that are offered by avalanche photodiodes. There are also Si alternatives that might provide better performance than the BPW34. InGaAs diodes are often used in telecommunication due to their stable, low-noise performance even at high frequencies. Their peak sensitivity is also usually in the red and infrared area of the light spectrum, which means the green light from the laser will be proportionally smaller than with the BPW34. Similar to avalanche photodiodes, the major drawback of InGaAs diodes is their price, which is much bigger than the BPW34. Some of the diode alternatives (InGaAs, avalanche and Si) that were explored as possible replacements for the BPW34 were the Hamamatsu G6854-01, Hamamatsu G17190-003K, Luna PDU-V104, OSI FCI-InGaAs-1000 and Marktech MTAPD-06-009. A cheaper alternative is the OSRAM SFH 203 FA, which detects less green light, has a lower dark current and has better directional characteristics, possibly leading to less ambient light detection. In spite of the improved characteristics, their impact will most likely be marginal.

Additionally there are ways to improve performance without modifying the circuit. The simplest way to increase the **SNR** is to move the setup to the dark room in the laboratory. Doing this will result in less ambient light being picked up by the photodiode. For future implementations that are interested in decreasing the size of the setup, an enclosure should be designed. This way, the main noise source will be the dark current.

Appendix A

Code

```

1 % requirements
2 V_o_tia = .5; % out voltage of tia
3 V_o = 5; % out voltage of non-inverting amp
4
5 % OPA795 specs
6 GBW = 1.5*10^6;
7 A_o_dB = 100; % DC open-loop gain in dB
8 A_o = 10^(A_o_dB/20); % DC open-loop gain
9 f_o = GBW/A_o; % open-loop cutoff frequency
10
11 % BPW34 specs
12 I_f = 50*10^-9; % max current from diode
13 C_d = 25*10^-12; % diode capacitance
14
15 % parasitic capacitances
16 C_cm = 2.2*10^-12; % common-mode capacitance
17 C_df = 2*10^-12; % differential capacitance
18 C_i = C_d + C_cm + C_df; % total parasitic capacitance
19
20 % R1 calculations
21 gain = V_o_tia/I_f;
22 gain_db = 20*log10(gain); % uncomment if you need gain in dB
23 R_1 = gain*(1 + A_o)/A_o;
24 %R_1 = 10e6; % realistic value for BPW34
25
26 % C1 calculation
27 omega_o = 2*pi*f_o;
28 C_1_num = -2*omega_o*R_1*C_i + 1 + sqrt(12*A_o*C_i*R_1*omega_o - 3);
29 C_1_den = 2*omega_o*R_1*(1 + A_o);
30 C_1 = C_1_num/C_1_den;
31
32 % system transfer function
33 divisor = (C_i + C_1)*R_1; % normalization coefficient
34 num = A_o*omega_o/divisor; % numerator
35 s1 = (1 + omega_o*R_1*(C_i + (1 + A_o)*C_1))/divisor; % first-order s
36 s0 = omega_o*(1 + A_o)/divisor; % zero-order s
37 den = [1, s1, s0];
38 tia = tf(num, den);
39 Q = sqrt(s0)/s1;
40
41 % cutoff calculations
42 omega_c = bandwidth(tia);
43 f_c = omega_c/(2*pi);
44
45 % noise transfer function
46 num = A_o*omega_o*[1 1/divisor];
47 s1 = 1/divisor + omega_o*(1 + A_o*C_1*(C_1 + C_i));
48 s0 = omega_o*(1 + A_o)/divisor; % 0th order term remains the same
49 den = [1 s1 s0];
50 tia_noise = tf(num, den);
51 tia_noise1 = tia_noise;

```

Figure A.1: TIA calculations

```

1 % results and plots
2 disp('Component values')
3 disp('R1: ' + R_1/10^6 + ' MΩ')
4 disp('C1: ' + C_1*10^12 + ' pF')
5 disp('System characteristics')
6 disp('fc = ' + f_c/10^3 + ' kHz = ' + omega_c/10^3 + ' krad/s')
7 disp('Q (actual): ' + Q)
8 disp('Q (ideal) : ' + 1/sqrt(3) + ' = sqrt(3)/3')
9 % bode plot system
10 figure
11 opts = bodeoptions;
12 opts.FreqUnits = 'Hz';
13 opts.Title.String = 'Frequency response';
14 bodeplot(tia, {10, 10^6}, opts);
15 % impulse plot system
16 figure
17 ip = impulseplot(tia);
18 % bode plot noise
19 figure
20 opts_n = bodeoptions;
21 opts_n.FreqUnits = 'Hz';
22 opts_n.Title.String = 'Noise frequency response';
23 bodeplot(tia_noise, {10, 10^6}, opts_n);
24 grid on

```

Figure A.2: Plots of the TIA calculations

```

1 % values from the TIA calculation script
2 R_1 = 10e6; % transimpedance (DC component)
3 V_o_tia = .5; % out voltage of tia
4 V_o = 5; % out voltage of non-inverting amp
5
6 V_cc = 5; % positive rail
7 V_ee = -5; % negative rail
8 I_q_a = 1.5e-3; % maximum quiescent current of AD795
9 I_q_b = 0.8e-3; % maximum quiescent current of AD820
10 R_2 = 11e3; % see report
11 R_3 = 110e3; % see report
12
13 % TIA-stage power
14 I_f_a = V_o_tia/R_1;
15 P_l_a = (V_cc - V_o_tia)*I_f_a; % load power
16 P_q_a = (V_cc - V_ee)*I_q_a; % quiescent power
17 P_a = P_l_a + P_q_a; % total power
18
19 % NIA-stage power
20 I_f_b = (V_o - V_o_tia)/R_3;
21 P_l_b = (V_cc - V_o)*I_f_b; % load power
22 P_q_b = (V_cc - V_ee)*I_q_b; % quiescent power
23 P_b = P_l_b + P_q_b; % total power
24
25 % R2 power
26 P_R2 = V_o_tia*I_f_b;
27
28 % total power
29 P = P_a + P_b + P_R2;
30 I = P/(V_cc - V_ee);
31 disp('TIA power : ' + P_a*10^3 + ' mW')
32 disp('NIA power : ' + P_b*10^3 + ' mW')
33 disp('R2 power : ' + P_R2*10^3 + ' mW')
34 disp('Total power : ' + P*10^3 + ' mW')
35 disp('Supply current: ' + I*10^3 + ' mA')
```

Figure A.3: Power calculation

```

1 tp = 20e-6; % pulse duration
2 scaling_f = 1500;
3 td = 10; % normalized dark time
4 T = scaling_f * tp; % period
5 t = 1:scaling_f;
6 y = zeros(1, length(t));
7 y(1) = 1; % init pulse cancel
8 y(scaling_f/2 + 1) = 1; % init pulse
9 y(scaling_f/2 + td + 1) = 1; % readout pulse
10 plot(t, y)
11 writematrix(y, 'pulse_20usD.csv')
12 disp('Pulse duration : ' + tp*10^6 + ' us')
13 disp('Dark time : ' + td*10^6*tp + ' us')
14 disp('Sequence period : ' + T*10^3 + ' ms')
```

Figure A.4: Power calculation

Glossary

AC Alternating Current 51

DC Direct Current 22, 24, 30, 38, 40–42, 44, 46

ECAD Electronic Computer-Aided Design 6, 35, 36

ESR Equivalent Series Resistance 26, 47

FET Field-Effect Transistor 23

GBP Gain-Bandwidth Product 20, 26, 28, 35, 52

GUI Graphical User Interface 6

IC Integrated Circuit 16, 25, 26

KCL Kirchhoff's Current Law 22

MRI Magnetic Resonance Imaging 11

MW Microwave 5, 6

NV Nitrogen Vacancy 5, 6, 8, 10–12, 14, 39, 47

ODMR Optically Detected Magnetic Resonance 4, 5, 58

CW-ODMR Constant-Wave ODMR 4–6, 11–13, 20, 22, 26, 28, 29, 33–35, 46, 51

P-ODMR Pulsed ODMR 5, 11, 13, 19, 28

OLIA Open Lock-In Amplifier 6–8, 37

PCB Printed Circuit Board 7, 8, 14, 20, 25, 34–36, 39, 47

PWM Pulse-Width Modulated 46

RF Radio-Frequency 39, 43

SNR Signal-to-Noise Ratio 8, 20, 53

SPICE Simulation Program with Integrated Circuit Emphasis 31

TIA Transimpedance Amplifier 14–17, 20, 21, 23, 24, 26–39, 47, 52, 53

TTL Transistor-Transistor Logic 5, 6, 13, 19

USB Universal Serial Bus 25

VNA Vector Network Analyzer 39, 43, 47

Bibliography

- [1] Wikipedia contributors, *Nitrogen-vacancy center — Wikipedia, the free encyclopedia*, [Online; accessed 3-September-2025], 2025. [Online]. Available: https://en.wikipedia.org/w/index.php?title=Nitrogen-vacancy_center&oldid=1301369588.
- [2] Wikipedia contributors, *Photoluminescence — Wikipedia, the free encyclopedia*, <https://en.wikipedia.org/w/index.php?title=Photoluminescence&oldid=1309081879>, [Online; accessed 4-September-2025], 2025.
- [3] Wikipedia contributors, *Optically detected magnetic resonance — Wikipedia, the free encyclopedia*, https://en.wikipedia.org/w/index.php?title=Optically_detected_magnetic_resonance&oldid=1301371272, [Online; accessed 6-October-2025], 2025.
- [4] V. K. Sewani et al., “Coherent control of nv- centers in diamond in a quantum teaching lab,” *American Journal of Physics*, vol. 88, no. 12, pp. 1156–1169, 2020.
- [5] A. Haque and S. Sumaiya, “An overview on the formation and processing of nitrogen-vacancy photonic centers in diamond by ion implantation,” *Journal of Manufacturing and Materials Processing*, vol. 1, no. 1, p. 6, 2017.
- [6] A. J. Harvie and J. C. de Mello, “Olia: An open-source digital lock-in amplifier,” *Frontiers in Sensors*, vol. 4, p. 1102176, 2023.
- [7] Z. Song et al., “Enhancing fluorescence of diamond nv- centers for quantum sensing: A multi-layer optical antireflection coating,” *Diamond and Related Materials*, vol. 141, p. 110584, 2024.
- [8] S. Saijo et al., “Ac magnetic field sensing using continuous-wave optically detected magnetic resonance of nitrogen-vacancy centers in diamond,” *Applied Physics Letters*, vol. 113, no. 8, 2018.
- [9] Y. Zhang et al., “High-sensitivity dc magnetic field detection with ensemble nv centers by pulsed quantum filtering technology,” *Optics Express*, vol. 28, no. 11, pp. 16191–16201, 2020.
- [10] J. Jones, W. Howden, A. Murphy, et al., *T1 relaxation time*. [Online]. Available: <https://doi.org/10.53347/rID-25821>.
- [11] D. Sitnic, *Internship technical report: Nitrogen-vacancy center setup*, Saxion Applied Nanotechnology research group, 2024.
- [12] *Silicon pin photodiode*, 81521, Rev. 2, Vishay, Aug. 2011.
- [13] *Photodiode characteristics and applications*. [Online]. Available: <https://osiptoelectronics.com/media/pages/knowledgebase/b954012b64-1675100541/an-photodiode-parameters-and-characteristics.pdf>.
- [14] P. Semig, *Transimpedance amplifier circuit*. [Online]. Available: <https://www.ti.com/lit/an/sboa268b/sboa268b.pdf>.
- [15] Z. Instruments, “Principles of lock-in detection and the state of the art. 2016,” *Internetadresse: https://www.zhinst.com/sites/default/files/li_primer/zi_whitepaper_principles_of_lock-in_detection.pdf*. Zuletzt aufgerufen am, vol. 17, 2018.
- [16] B. Acharya, “Compact integration of nv-based diamond quantum sensors using a small-size photodiode and on-board transimpedance amplifier,” Ph.D. dissertation, Wichita State University, 2025.
- [17] B. Black and G. Brisebois, *Transimpedance amplifiers for wide range photodiodes have challenging requirements*, 2021.
- [18] *Ad795; low power, low noise precision fet op amp*, Rev. D, Analog Devices, 2019.
- [19] *Ad820; single-supply, rail-to-rail, low power, fet input op amp*, Rev. H, Analog Devices, 2011.

- [20] *Noise analysis in operational amplifier circuits*, SLVA043B, Rev. 2, Texas Instruments, 2007.
- [21] K. Asparuhova and E. Gadjeva, “Noise analysis of operational amplifier circuits using matlab,” in *27th International Spring Seminar on Electronics Technology: Meeting the Challenges of Electronics Technology Progress, 2004.*, vol. 3, 2004, 471–475 vol.3. DOI: [10.1109/ISSE.2004.1490859](https://doi.org/10.1109/ISSE.2004.1490859).
- [22] E. Margan, “Transimpedance amplifier analysis,” *no*, vol. 1, pp. 1–19, 2012.
- [23] E. Säckinger, *Analysis and design of transimpedance amplifiers for optical receivers*. John Wiley & Sons, 2017.
- [24] L. Horsthemke et al., “All optical magnetometry with nitrogen vacancy centers in diamonds,” Ph.D. dissertation, Universidad de Granada, 2025.
- [25] S. Cherian, “What you need to know about transimpedance amplifiers—part 1,” *Texas Instruments Incorporated*, 2016.
- [26] L. Clark, *Adafruit tps65131 split power supply boost converter*, 2025. [Online]. Available: <https://cdn-learn.adafruit.com/downloads/pdf/adafruit-tps65131-split-power-supply-boost-converter.pdf>.
- [27] *Tps65133 ±5-v, 250-ma dual-output power supply*, SLVSC01A, Rev. A, Texas Instruments, Jun. 2013.
- [28] TangentSoft. “Virtual ground circuits.” [Online]. Available: <https://tangentsoft.com/elec/vgrounds.html>.
- [29] T. Instruments, *Tps6040x unregulated 60-ma charge pump voltage inverter*, 2015.
- [30] C. Hoyle and A. Peyton, “Bootstrapping techniques to improve the bandwidth of transimpedance amplifiers,” in *IEE Colloquium on Analog Signal Processing (Ref. No. 1998/472)*, IET, 1998, pp. 7–1.
- [31] C. Hoyle and A. Peyton, “Shunt bootstrapping technique to improve bandwidth of transimpedance amplifiers,” *Electronics Letters*, vol. 35, no. 5, pp. 369–370, 1999.
- [32] S. Idrus, N. Ngajikin, N. Malik, and S. Aziz, “Performance analysis of bootstrap transimpedance amplifier for large windows optical wireless receiver,” in *2006 International RF and Microwave Conference*, IEEE, 2006, pp. 416–420.
- [33] *Cascading precision op amp stages for optimal ac and dc performance*, SBOA356, Texas Instruments, Aug. 2020.
- [34] *Ada4627-1/ada4637-1; 30 v, high speed, low noise, low bias current, jfet operational amplifier*, Rev. F, Analog Devices, 2015.
- [35] B. Razavi, “The transimpedance amplifier [a circuit for all seasons],” *IEEE Solid-State Circuits Magazine*, vol. 11, no. 1, pp. 10–97, 2019.
- [36] *Opa818 2.7ghz, high-voltage, fet-input, low-noise, operational amplifier*, SBOS940B, Rev. B, Texas Instruments, 2019.
- [37] D. Santiago, *A high-speed transimpedance amplifier*, 2021. [Online]. Available: https://cmosedu.com/jbaker/students/david/myStuff/LinkPages/Projects/ECG720_SANTIAGO_PROJECT_S21.pdf.
- [38] A. Karimi-Bidhendi, H. Mohammadnezhad, M. M. Green, and P. Heydari, “A silicon-based low-power broadband transimpedance amplifier,” *IEEE Transactions on Circuits and Systems I: Regular Papers*, vol. 65, no. 2, pp. 498–509, 2017.
- [39] B. Analui and A. Hajimiri, “Bandwidth enhancement for transimpedance amplifiers,” *IEEE Journal of Solid-State Circuits*, vol. 39, no. 8, pp. 1263–1270, 2004.